

Novel anisotropic teleseismic body-wave tomography code AniTomo to illuminate heterogeneous anisotropic upper mantle: Part II – Application to data of passive seismic experiment LAPNET in northern Fennoscandia

Helena Munzarová¹, Jaroslava Plomerová,¹ Eduard Kissling,² Luděk Vecsey¹ and Vladislav Babuška¹

¹ Institute of Geophysics, Academy of Sciences, Prague, Czech Republic. E-mail: helena@ig.cas.cz

² Institute of Geophysics, Department of Earth Sciences, ETH Zürich, Switzerland

Accepted 2018 August 3. Received 2018 June 27; in original form 2018 February 15

SUMMARY

Seismic anisotropy provides a unique constraint on the past and present dynamics of the lithosphere and sublithospheric mantle. To contribute to studies of large-scale tectonic fabric, we have developed code AniTomo for regional anisotropic tomography. AniTomo allows us to invert simultaneously relative traveltimes residuals of teleseismic P waves for 3-D distribution of isotropic-velocity perturbations and velocity anisotropy in the upper mantle. Weak hexagonal anisotropy with the symmetry axis oriented generally in 3-D is considered.

The first application of novel code AniTomo to data from passive seismic experiment LAPNET results in a model of anisotropic velocities of the upper mantle beneath northern Fennoscandia. We have opted for northern Fennoscandia for the first application because it is a tectonically stable Precambrian region with a thick anisotropic mantle lithosphere without significant thermal heterogeneities. We carefully analyse the distribution of the rays to limit the fully anisotropic inversion only to the volume with the sufficient directional ray coverage. Capability of the given inversion setup to reveal large-scale anisotropic structures in the upper mantle is documented by a series of synthetic tests.

The strongest anisotropy and the largest velocity perturbations concentrate at depths corresponding to the mantle lithosphere, while in deeper parts of the tomographic model, the lateral variations are insignificant. We delimit regions of laterally and vertically consistent anisotropy in the mantle–lithospheric part of the model. We attribute the retrieved domain-like anisotropic structure of the mantle lithosphere in northern Fennoscandia to preserved fossil fabrics of the Archean microplates, accreted during the Precambrian orogenic processes.

Key words: Body waves; Seismic anisotropy; Seismic tomography; Dynamics of lithosphere and upper mantle.

1 INTRODUCTION

Deciphering fabrics of the upper mantle is an important task for back-in-time reconstruction of development of the continental lithosphere (see for a review of anisotropy, e.g. Babuška & Cara 1991; Šílený & Plomerová 1996; Silver 1996; Savage 1999; Park & Levin 2002; Babuška & Plomerová 2006; Fouch & Rondenay 2006; Mainprice 2007; Maupin & Park 2007; Long & Silver 2009; Long & Becker 2010). Shear and surface waves enable to study smooth and long-wavelength variations of the large-scale velocity anisotropy, resulting in azimuthal- or radial-anisotropy shear-velocity models of the upper mantle (e.g. Panning & Romanowicz 2006; Kustowski *et al.* 2008; Fichtner *et al.* 2010, 2013; Auer *et al.* 2014; French &

Romanowicz 2014; Yuan & Beghein 2014; Zhu *et al.* 2014; Chang *et al.* 2015; Debayle *et al.* (2016); Ho *et al.* 2016; Nita *et al.* 2016). On the other hand, teleseismic P waves are sensitive to smaller-scale structures due to their shorter wavelengths and they represent independent data. Hammond & Toomey (2003) use teleseismic P - and S -wave delay times and shear-wave splitting measurements to constrain isotropic and anisotropic heterogeneity in the mantle beneath the southern East Pacific Rise. Systematic studies of seismic anisotropy in various continental provinces document spatial variation of directional terms of relative P -wave traveltimes residuals and dependence of shear-wave splitting parameters on backazimuth (e.g. Babuška *et al.* 1993; Babuška & Plomerová 2006; Plomerová *et al.* 2011, 2012). The authors interpret such anisotropic signatures

of the body waves by anisotropy with a general orientation of the symmetry axes within blocks, or domains, of mantle lithosphere.

Neglecting seismic anisotropy and considering only isotropic wave propagation in teleseismic body-wave tomography of the upper mantle is a simplification that is incompatible with current understanding of the plate tectonics and upper mantle dynamics. Ignoring seismic anisotropy can potentially bias the resulting isotropic-velocity models (e.g. Bezada *et al.* 2016) and mask true fabrics of the Earth structures. Different approaches of inverting *P*-wave traveltimes or traveltimes deviations for anisotropic velocities can be found in various tomographic applications (e.g. Hirahara & Ishikawa 1984; Ishise & Oda 2005; Wang & Zhao 2013), but most of them are limited to the crust, using local-earthquake data sets and searching for azimuthal anisotropy only. On the other hand, for example Liu & Zhao (2017) or Hua *et al.* (2017) evaluate also radial anisotropy from local-earthquake data sets merged with teleseismic data sets, but the separation of radial and azimuthal anisotropy yet represents a significant simplification of the true anisotropic structure of the Earth.

To contribute to studies of large-scale anisotropy of the upper mantle, we have developed a unique code, called AniTomo, for regional anisotropic *P*-wave tomography (Munzarová *et al.* 2018). AniTomo inverts traveltimes residuals of teleseismic *P* waves simultaneously for 3-D distribution of isotropic velocity perturbations and anisotropy in the upper mantle. This tomographic code represents a step further from modelling homogeneously anisotropic blocks of mantle lithosphere (e.g. Babuška *et al.* 1993; Šílený & Plomerová 1996; Vecsey *et al.* 2007) towards modelling the upper mantle with arbitrarily varying anisotropy in 3-D. AniTomo assumes a weak anisotropy of the hexagonal symmetry with axes oriented generally in 3-D and it is the first tomographic code that includes inclination of the axes among the model parameters. Allowing for the fully 3-D orientation of the symmetry axes is crucial to model successfully anisotropic fabric of individual domains of the continental mantle lithosphere. The theoretical background of the AniTomo code is presented in a methodological paper by Munzarová *et al.* (2018). The paper also includes many synthetic tests of resolution, separation of the isotropic and anisotropic model parameters, their convergence to the true values and discussion of effects of inversion setup on the results.

For the first application of the AniTomo code to a real data set, we have selected data from international passive seismic experiment POLENET/LAPNET deployed in northern Fennoscandia (2007–2009; e.g. Kozlovskaya 2007). The Fennoscandian Shield is an assemblage of microplate nuclei, island arcs, terranes and mobile belts of prevailingly Archean age in the northeast and of Proterozoic age in the southwest (e.g. Snyder 2002; Korja *et al.* 2006; Lahtinen *et al.* 2015). We focus on the northern part of Fennoscandia, where Archean cratons, that is Karelia, Kola and Norrbotten, accreted together with Belomorian Mobile Belt and various arcs and terranes during the Lapland-Kola and Lapland-Savo orogenies in the Palaeoproterozoic (e.g. Korja *et al.* 2006). At present, northern Fennoscandia is a tectonically stable region with a relatively thick lithosphere (Plomerová & Babuška 2010) and without significant thermal heterogeneities (e.g. Slagstad *et al.* 2009, for a review).

Seismological research of the upper mantle beneath northern Fennoscandia has flourished particularly after the POLENET/LAPNET experiment that complemented sparsely distributed permanent observatories equipped with broad-band seismometers. Various types of data from the experiment, processed

by different techniques, provide new information on velocity structure and discontinuities in the upper mantle, for example from inversion of dispersion curves of Rayleigh waves (Pedersen *et al.* 2013) and from joint inversion of *P* and *S* receiver functions (Vinnik *et al.* 2016). Teleseismic *P*-wave traveltimes were analysed to assess thickness of the lithosphere at around 150 km (e.g. Plomerová & Babuška 2010). Silvennoinen *et al.* (2016) evaluated a tomographic model of isotropic-velocity perturbations of the upper mantle (see Section 5.2 for a comparison of the tomographic models). Plomerová *et al.* (2011) delimited domains of uniform large-scale anisotropy with the symmetry axes oriented generally in 3-D within the mantle lithosphere by joint interpretation of *P*- and SKS-wave anisotropic characteristics. Azimuthal anisotropy and its depth dependence within the upper mantle were studied by Vinnik *et al.* (2014) by a joint inversion of SKS splitting parameters and *P* receiver functions.

In this paper, we present a 3-D model of the upper mantle beneath northern Fennoscandia, in which we show *P*-wave isotropic-velocity perturbations and anisotropic parameters retrieved with the novel coupled anisotropic-isotropic tomography code AniTomo. Furthermore, the results are complemented with a series of synthetic inversions to test resolution capability of the LAPNET ray geometry and analysed along with the previous independent findings of anisotropic structure of the region (Plomerová *et al.* 2011).

2 DATA AND THEIR PRE-PROCESSING FOR ANISOTROPIC TOMOGRAPHY

Teleseismic *P*-wave arrival times measured on recordings of the LAPNET array represent a core of the data set for anisotropic tomography of the upper mantle beneath northern Fennoscandia calculated with code AniTomo. POLENET/LAPNET was a subproject of the POLENET-IPY consortium (Cooper *et al.* 2008) related to seismic and geodetic studies in the Arctic regions, which included also tomographic studies of velocity structure of the upper mantle beneath northern Fennoscandia.

Seismic array LAPNET (e.g. Kozlovskaya 2007; <http://www.oulu.fi/sgo-oty/lapnet/>; http://www.fdsn.org/networks/detail/XK_2007/) was installed on the territory of northern Finland and Finnmark area of Norway, and neighbouring northwestern Russia between May 2007 and September 2009 (see also Plomerová *et al.* 2011). The original array consisted of ~37 temporary broad-band stations (LP00-LP83) and observatories of the Northern Finland Seismological Network (OUL, SGF, MSF, RNF), the Helsinki University Seismic Network (KU6, VRF, HEF, KEV, KIF) and neighbouring stations in Norway (KTK1). For this study, we enlarge the data set by *P*-wave arrival times measured on ten permanent stations of the Swedish National Seismological Network located westward of the LAPNET array (KUR, NIK, MAS, DUN, LAN, PAJ, ERT, SAL, KAL, HAR; SNSN 1904) and two more stations to the north belonging to the Norwegian seismic networks (ARE0, TRO). This step represents 25 per cent enlargement of the original LAPNET array. The extended array covers an area of about 500 km by 500 km with average interstation spacing of 70 km (Fig. 1).

We select recordings of 90 earthquakes from teleseismic epicentral distances between 20° and 100° (Fig. 2) and measure arrival times of *P* waves on seismograms with 20 Hz sampling simula-

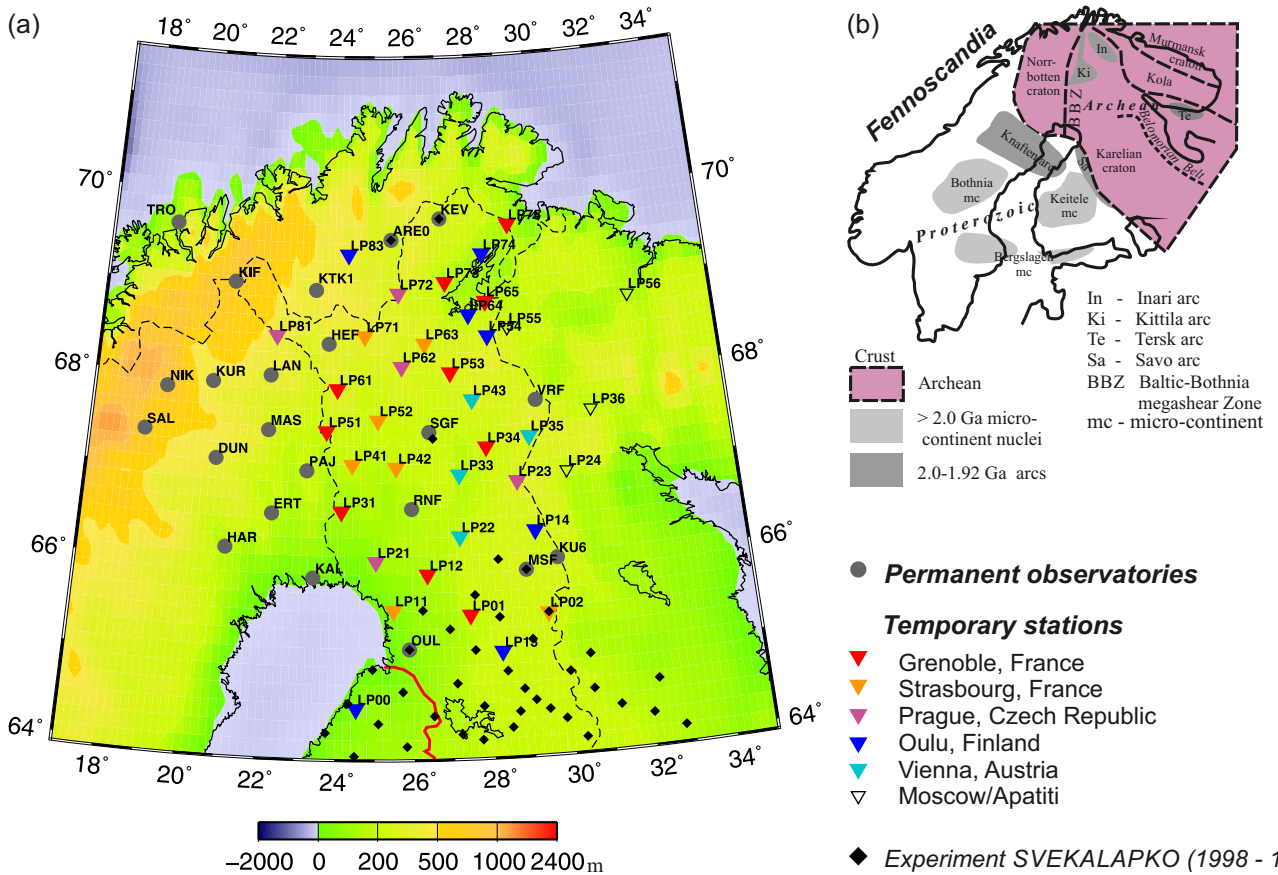


Figure 1. Permanent and temporary seismic stations deployed during passive seismic experiment LAPNET (2007–2009) in northern Fennoscandia (a). Distribution of microcontinental nuclei, island arcs and boundaries of hidden and exposed terranes older than 1.92 Ga in the Fennoscandian Shield (b), redrawn according to Korja *et al.* (2006).

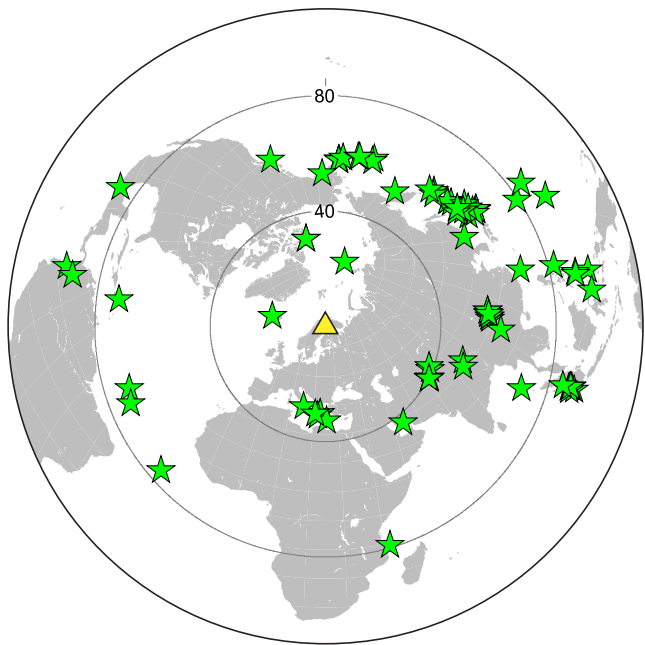


Figure 2. Location of 90 teleseismic events (green stars) recorded by the LAPNET array (yellow triangle) and selected for the teleseismic P -wave arrival-time measurements.

ing the WWSSN-SP response with the use of a semi-automatic picker developed by Vecsey (private communication 2010), based on Seismic Handler (Stammler 1993). Because we invert for velocity structure of the upper mantle, we correct the measured traveltimes for differences between a model of the Fennoscandian crust and reference radial velocity model of the Earth IASP'91 (Kennett & Engdahl 1991). We have tested several crustal models and we use a recent model by Silvennoinen *et al.* (2014) for the final calculations.

Data pre-processing for the inversion includes a calculation of absolute traveltimes residuals, that is differences between the observed traveltimes and the theoretical traveltimes for reference model IASP'91. To minimize effects originated outside the volume studied, we calculate relative residuals by subtracting an event average residual from the absolute residuals of each event. We also test time stability of the relative residuals to avoid potential operational problems, for example occasional failures of the time synchronization at some of the temporary stations. Finally, the input P -wave data set for tomography consists of 3286 relative traveltimes residuals, which all lie in an interval of (-2 s; 2 s), out of which 96 per cent are in an interval of (-0.5 s; 0.5 s). Such a low variability of the traveltime residuals excludes a strong large-scale heterogeneity in the upper mantle beneath northern Fennoscandia.

3 METHOD

3.1 AniTomo—theoretical background

We use novel anisotropic code AniTomo (Munzarová *et al.* 2018) to invert the relative traveltimes residuals of teleseismic P waves jointly for both the isotropic-velocity perturbations and velocity anisotropy of the upper mantle beneath northern Fennoscandia. We have developed AniTomo as a modification of code Telinv that is broadly used for standard isotropic-velocity teleseismic tomography (e.g. Weiland *et al.* 1995; Arlitt *et al.* 1999; Lippitsch *et al.* 2003; Sandoval *et al.* 2004; Shomali *et al.* 2006; Eken *et al.* 2007; Karousová *et al.* 2012, 2013; Karousová 2013; Plomerová *et al.* 2016; Silvennoinen *et al.* 2016; Chyba *et al.* 2017). Weak anisotropy models with hexagonal symmetry both with the high-velocity a -axis or with the low-velocity b -axis, generally oriented in 3-D, are allowed. The medium is described by the isotropic (average) component \bar{v} of the anisotropic velocity v , strength of anisotropy k and two angles for orientation of the symmetry axis—azimuth λ and inclination θ . Then, the formula for P -wave velocity v in a weakly anisotropic medium with hexagonal symmetry can be written as

$$v = \bar{v} \left\{ 1 + k \left[(\sin i \sin \theta \cos(\phi - \lambda) + \cos i \cos \theta)^2 - \frac{1}{2} \right] \right\}, \quad (1)$$

where ϕ and i are backazimuth and incidence angles defining the propagation of the wave in 3-D. In general, AniTomo is applicable only to P waves and not to S waves, whose anisotropic propagation is more complex.

We have linearized the relation between the traveltime residual Δt and perturbations of anisotropic parameters $\Delta \bar{v}$, Δk , $\Delta \lambda$ and $\Delta \theta$ at each grid node (indexed with j)

$$\begin{aligned} \Delta t = & \sum_j \left(\frac{\partial t}{\partial \bar{v}} \right)_j \Delta \bar{v}_j + \sum_j \left(\frac{\partial t}{\partial k} \right)_j \Delta k_j \\ & + \sum_j \left(\frac{\partial t}{\partial \lambda} \right)_j \Delta \lambda_j + \sum_j \left(\frac{\partial t}{\partial \theta} \right)_j \Delta \theta_j, \end{aligned} \quad (2)$$

which leads to a system of linear equations that we solve with damped least-square method (e.g. Menke 1984)

$$\mathbf{m} = (\mathbf{A}^T \mathbf{W}_D \mathbf{A} + \epsilon^2 \mathbf{W}_M)^{-1} \mathbf{A}^T \mathbf{W}_D \mathbf{d}, \quad (3)$$

where \mathbf{m} is vector of model parameters $\Delta \bar{v}$, Δk , $\Delta \lambda$ and $\Delta \theta$ at all nodes. Data vector \mathbf{d} contains traveltimes residuals Δt and matrix \mathbf{A} stores the partial derivatives from eq. (2). Errors of arrival-time measurements are considered in weighting matrix \mathbf{W}_D . Damping factor ϵ^2 stabilizes the ill-posed problem. Independent values of damping must be set for the four types of parameters describing the medium. Horizontal smoothing of model parameters can be achieved via matrix \mathbf{W}_M . The inverse in eq. (3) is approximated by truncated singular value decomposition. 3-D ray tracing bending technique Simplex (Steck & Prothero 1991), in which ray paths are distorted by sinusoidal signals, is applied. Reliability of the model parameters for a given ray distribution and inversion setup can be assessed with resolution matrix \mathbf{R}

$$\mathbf{R} = (\mathbf{A}^T \mathbf{W}_D \mathbf{A} + \epsilon^2 \mathbf{W}_M)^{-1} \mathbf{A}^T \mathbf{W}_D \mathbf{A}, \quad (4)$$

or, with ray density tensors (see Section 3.2).

3.2 Setup of parameters controlling the inversion

We parametrize the volume studied with an orthogonal 3-D grid of nodes, at which the model parameters are searched during the

inversion. After a series of inversion runs, we have selected a regular horizontal grid spacing of 70 km \times 70 km. For a smaller spacing between the nodes, the tomographic images disintegrate and they split into single-cell anomalies indicating an overparametrization. Vertical grid nodes are set at 20, 50 and 80 km depth to enhance separation of the mantle lithosphere and the crust. Further down, from 120 to 370 km the spacing is regular with a 50 km step. We do not invert below 370 km because of the decreasing resolution (see, e.g. Figs S1–S3). The ray coverage of the teleseismic data set is not, of course, sufficient to resolve the crustal structure. The Fennoscandian crust is thick and it is quite likely that an effect of the crust and its inner structure need not be fully eliminated by the crustal correction of the relative residuals. Therefore, we invert for isotropic-velocity perturbations at the 20 km depth to compensate the uncorrected crustal effects and to prevent their mapping into the mantle. But of course, we avoid any interpretation of the velocity perturbations at the 20 km depth.

AniTomo enables to invert for arbitrarily selected model parameters at each node. This means that we can search only for isotropic-velocity perturbations at nodes, where the directional distribution of the rays is not sufficient. Purely isotropic inversion in the whole volume is also possible with the code. Diagonal elements of the resolution matrix (RDE; eq. 4; Fig. S1) or ray segments (Fig. S2) show ray coverage at the individual depth layers. Smoothed contours of RDE equal to 0.5 are considered as a limit of the well-resolved part of the volume studied. The relatively small area delimited by the 0.5 contour of RDE at the 50 km depth is caused by smaller vertical spacing between the nodes in this part of the model. For the purpose of anisotropic tomography, we also evaluate so-called ray density tensors (RDT; Kissling 1988; Sandoval *et al.* 2004) to investigate spatial distribution of rays in each cell and according to that we restrict the fully anisotropic inversion only to the well-sampled nodes. Munzarová *et al.* (2018) describe evaluation of the RDT within the AniTomo code in detail.

As an example, Fig. 3 shows orientations of the RDT eigenvectors and sizes of the eigenvalues for nodes at the 120 km depth (see Fig. S3 for all the depth layers). The ray density tensors indicate not only an overall amount of rays within the parametrization cells by size of their eigenvalues, but they also graphically express quality of directional distribution of the rays by orientation of the eigenvectors and ratio between the eigenvalues. The steeper the orientation of the eigenvector belonging to the largest eigenvalue A (green or yellow dots), the more evenly teleseismic rays cover the parametrization cell. The most even distribution of the rays is in the central part of the individual depth layers (Figs 3 and S3), while towards the edges, the eigenvectors with the largest eigenvalue tend to be oriented in direction of prevailing ray orientations. Ratios of the smaller eigenvalues ($B1$ and $B2$) with respect to the largest eigenvalue, that is $B1*A^{-1}$ and $B2*A^{-1}$, express evenness of the directional coverage as well. Synthetic tests with a quasi-equal realistic distribution of stations and teleseismic events show that ratios $B1*A^{-1}$ and $B2*A^{-1}$ in a range from 0.1 to 0.2 are typical for teleseismic events. The eigenvalue ratios evaluated for the LAPNET data set reach similar values at many grid nodes (background colour in Figs 3 and S3). Though these values seem to be low, they guarantee a good recovery of the anisotropic parameters (Munzarová *et al.* 2018).

To define nodes where we can invert for anisotropy, we need to delimit a subregion with the highest number and the best directional distribution of the rays in each layer. According to the RDT, we define an irregular, but relatively smooth subregion at the 120 km depth, in which the inversion for all the four anisotropic parameters is allowed (space within the red line in Figs 3 and S3). Then, we limit

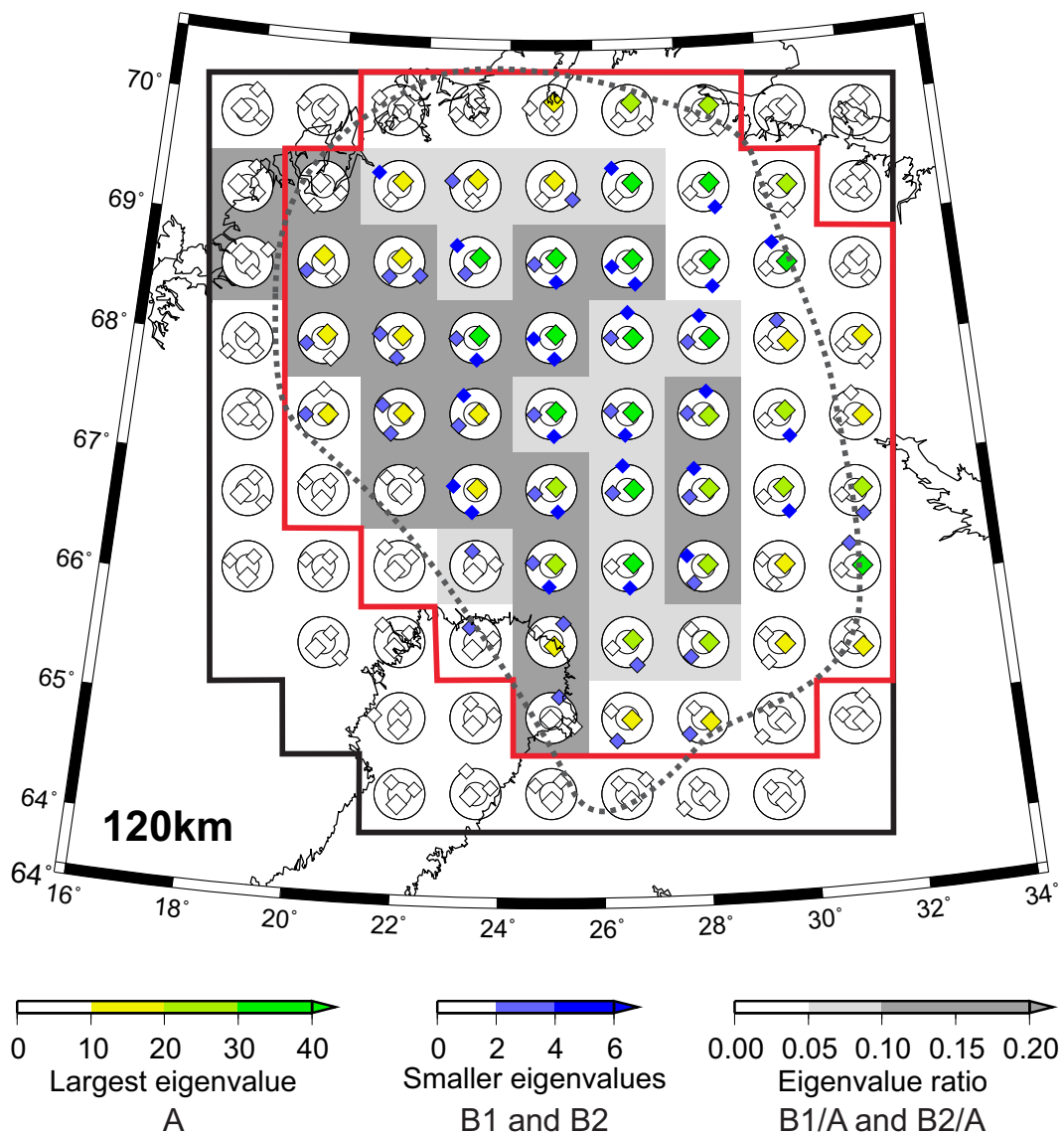


Figure 3. Ray density tensors (RDT) evaluated for the parametrization nodes of the 120 km depth for ray distribution of the LAPNET data set (see Fig. S3 for all the depth layers). We image orientation of three RDT eigenvectors of each node with points in the lower-hemisphere stereographic projection. Size of the largest RDT eigenvalue of a node (marked as A) is displayed with a different colour scale than size of the two smaller eigenvalues (marked as B1 and B2). Ratios between the smaller eigenvalues and the largest eigenvalue at a node, i.e. $B1 \cdot A^{-1}$ and $B2 \cdot A^{-1}$, are imaged with a background colour. Both the ratios at a node must be larger than the lower limit of a colour band to get the colour. Red line marks the region where inversion for all the four anisotropic parameters is allowed (at depth layers from 50 km down to 270 km). Inversion only for the purely isotropic-velocity perturbations is allowed in between the black and red lines at depths from 50 km to 270 km and within the black line at the 20 km, 320 km and 370 km depths. Smoothed contour of diagonal elements of the resolution matrix equal to 0.5 is imaged with dotted black curves.

the anisotropic inversion only to that subregion at every depth layer from 50 km down to 270 km. At nodes neighbouring the subregion at the 50–270 km depths (in between the black and red lines in Figs 3 and S3) and at all the nodes of the 20, 320 and 370 km depths (within the black line), we invert only for purely isotropic-velocity perturbations. Thus in total, we invert for 783 perturbations of isotropic-velocity components, 366 perturbations of strength of anisotropy, 366 perturbations of azimuth and 366 perturbations of inclination, that is 1881 unknown model parameters all together.

Well-tuned damping of a mixed-determined problem is also essential for a successful inversion. Damping affects the rate of convergence of the model parameters with number of iterations, their overall amplitude and scatter (for details see Munzarová *et al.* 2018). In

the case of azimuth and inclination of the symmetry axis, well-tuned damping factors are essential for stability of the inversion because of non-linearity between the angles and the anisotropic velocity (eq. 1). Perturbations of each of the four anisotropic parameters, that is isotropic component of velocity, strength of anisotropy, azimuth and inclination of the symmetry axis, have their own value of damping in AniTomo, of course, with a different physical meaning. In the case of LAPNET data, we choose value of 3 for damping of the perturbations of isotropic component of the velocity according to the trade-off curve evaluated from the purely isotropic inversions (Fig. 4). We achieve a good compromise between prediction error and solution length and physically reasonable amplitudes of the velocity perturbations for that damping within three iterations. For

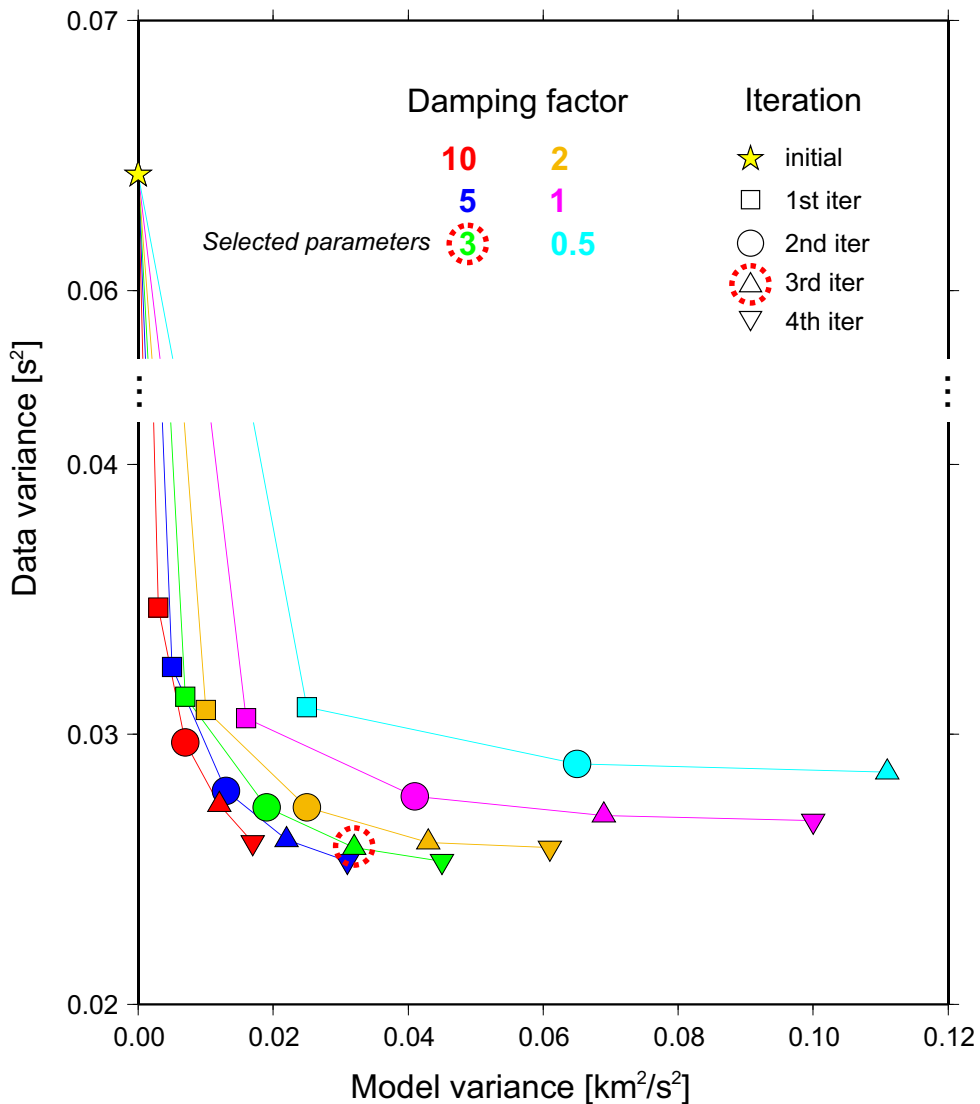


Figure 4. Data and model variance trade-off curve evaluated for various values of damping of the isotropic-velocity perturbations and numbers of iterations from purely isotropic inversions.

damping of perturbations of strength of anisotropy, and perturbations of azimuth and inclination of the symmetry axis, we select 100, 0.1 and 0.5, respectively, after testing various values on synthetic data. These values were chosen already for the series of methodological synthetic tests (Munzarová *et al.* 2018) and they seem to be appropriate also in the case of LAPNET ray geometry. They lead very well to smoothly converging model parameters with limited scatter.

3.3 Anisotropic inversion—initial models and visualization of the results

If the parameters controlling the inversion are well tuned, then purely isotropic-velocity modelling is a single run, including several iterations. On the other hand, evaluation of anisotropy with symmetry axes oriented generally in 3-D consists of a series of single anisotropic inversions that differ in the initial orientation of the symmetry axis (Munzarová *et al.* 2018). This is due to sensitivity

of the output anisotropic model to angular deviation between orientation of the symmetry axis of the initial and the target models. In the case of relatively small deviation between the axes ($<\sim 60^\circ$), regardless of *a* and *b* model types, the symmetry axis returned by the inversion converges to the correct orientation and the strength of anisotropy increases. But, if the initial axis orientation is approximately perpendicular to the target one, the solution converges to an anisotropic model with the other type of hexagonal symmetry and with the axis approximately perpendicular to the correct orientation. Despite the misinterpretation of the type of hexagonal symmetry, the directions of relatively high and low velocities are well captured when the anisotropy has inclined symmetry axes (Fig. 5a). Based on previous studies of anisotropy with the use of single station method (e.g. Babuška *et al.* 1993; Babuška & Plomerová 2006; Plomerová & Babuška 2010; Plomerová *et al.* 2012), we consider both the *a*-axis and *b*-axis models to approximate the continental mantle lithosphere structure. Discrimination between the models with the high-velocity *a* lineation, and models with the low-velocity *b*-axis

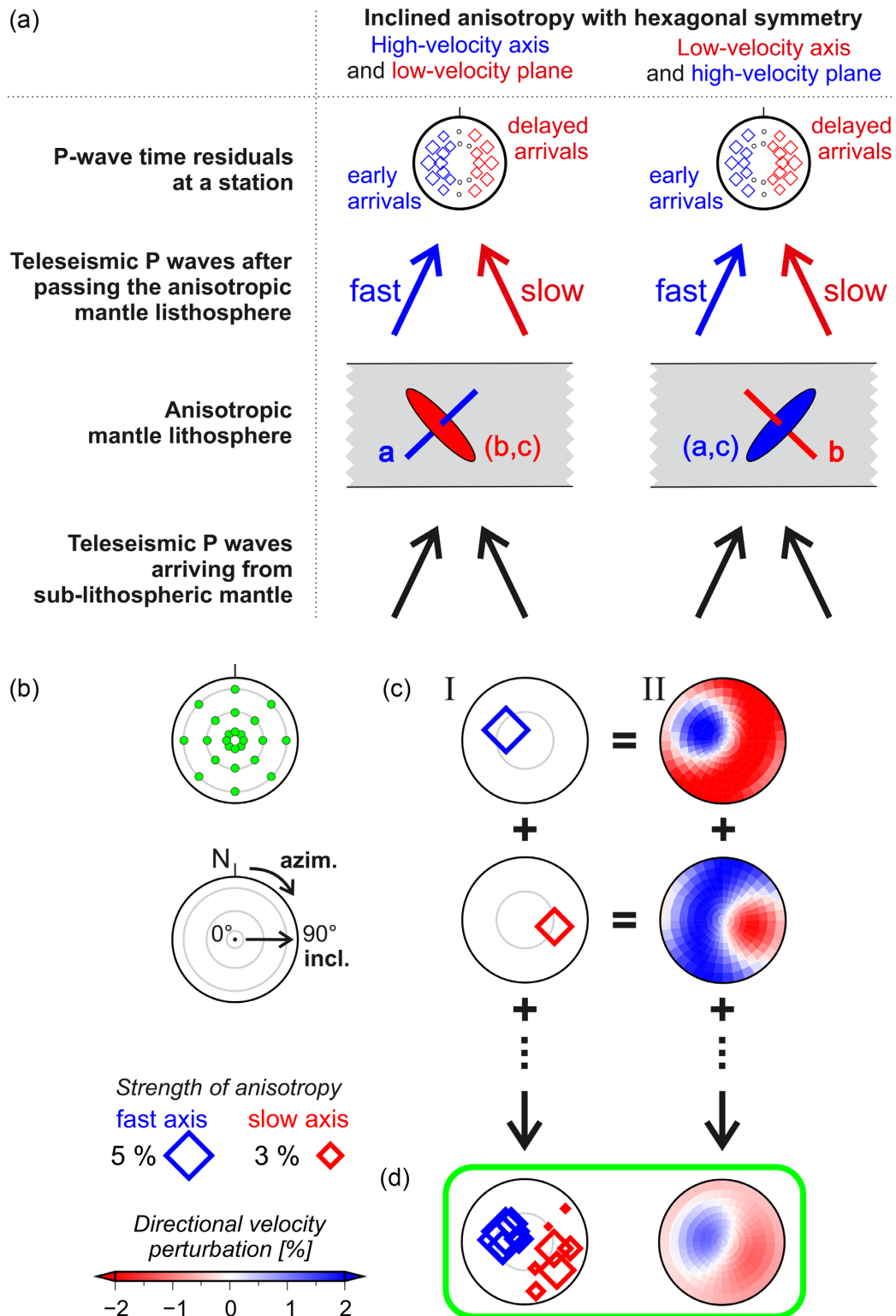


Figure 5. (a) A scheme illustrating influence of anisotropy with inclined symmetry axes on velocity of steeply propagating teleseismic P waves. The large-scale anisotropy of a mantle–lithospheric domain is approximated by models with hexagonal symmetry either with the high-velocity a axis and the low-velocity (b,c) plane (lineation), or, with the low-velocity b -axis and the high-velocity (a,c) plane (foliation). The P -sphere patterns evaluated for these two types of anisotropy illustrate directional variations of traveltime residuals relative to an isotropic background. (b) A set of 24 initial orientations of symmetry axis displayed in the lower-hemisphere stereographic projection. Azimuth (azim.) covers the 360° range with a step of 45° , while inclination (incl.) acquires values of 10° , 45° and 80° . (c) Two ways of visualization of an individual solution of anisotropy at a parametrization node, i.e. displaying either orientation of its hexagonal-symmetry axis and strength of anisotropy with a single point (I) or its directional distribution of relatively high and low P -wave velocities (II). (d) Plotting the individual solutions jointly (I) or averaging their velocity contributions for every direction (II), a final output model of anisotropy is constructed for each node.

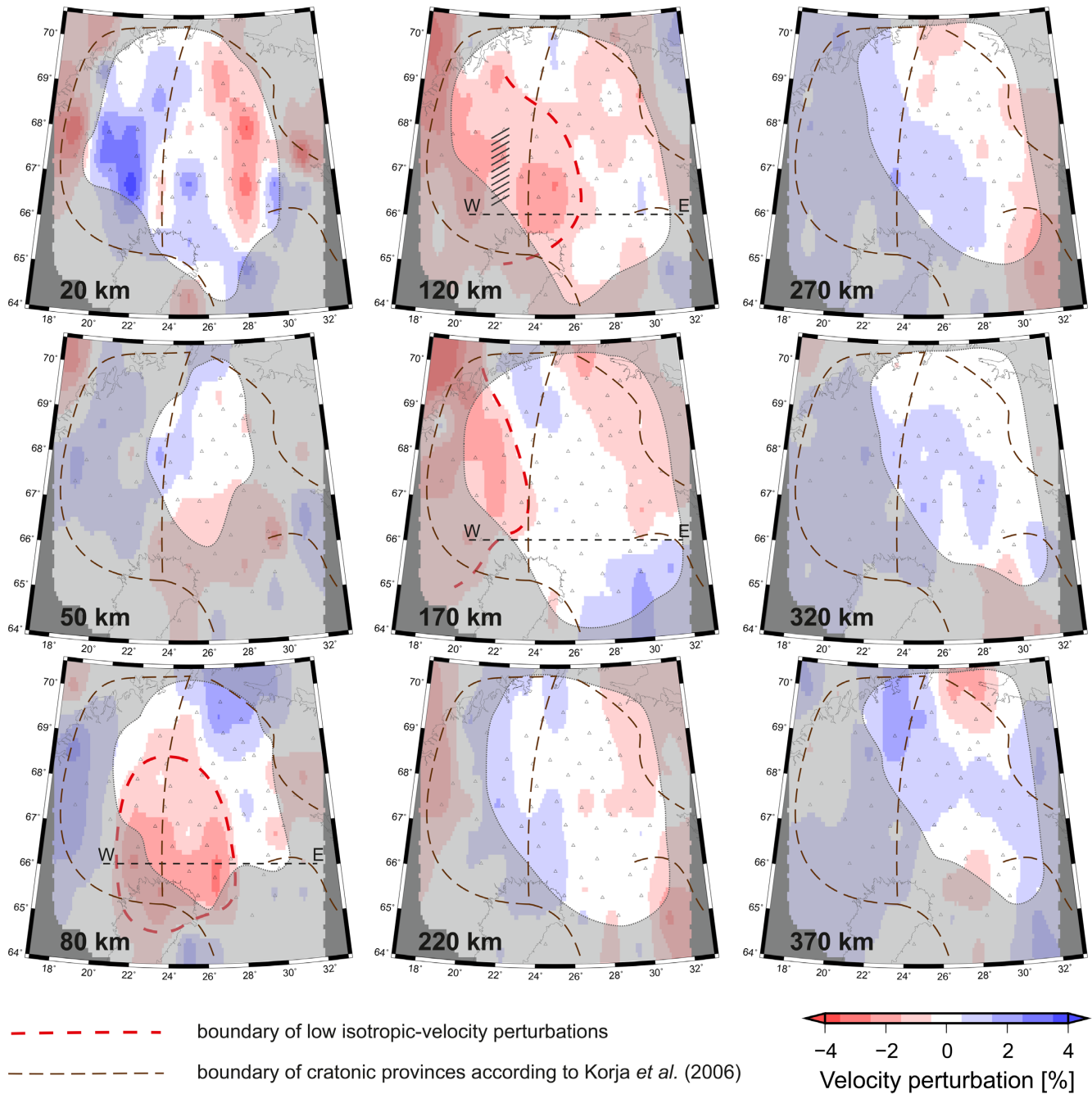


Figure 6. Perturbations of the isotropic velocity calculated as average values of the isotropic-velocity perturbations resulting from the series of the coupled anisotropic-isotropic inversions. See Fig. S11 for a vertical section along the AB profile and Figs R2 and S4 for the anisotropic part of the tomographic model. Part of the model with $RDE < 0.5$ is shaded. Red dashed line limits the relatively low-velocity perturbations that dominate western and southwestern parts of the model at depths of 80, 120 and 170 km. The hatched area marks a zone of weaker anisotropy and velocity perturbations within Region III at depth of 120 km. The brown dashed curves show boundaries of cratonic provinces after Korja et al. (2006); see also Fig. 1. Triangles represent seismic stations of experiment LAPNET together with the nearby permanent stations.

and high-velocity (*a,c*) foliation is in general subtle for the teleseismic *P* waves only. Additional information from independent data, for example shear-wave splitting parameters can help to differentiate between the two types of hexagonal symmetry (e.g. Plomerová *et al.* 2011).

To assure that the anisotropic tomography results in a correct unbiased model, we need to systematically cover the full range of initial orientations of the symmetry axis (Fig. 5b). Therefore, we repeat the inversion 24 times with gridded initial azimuth and

inclination within the volume studied. The initial azimuth changes with a step of 45° and the inclination subsequently acquires values of 10° , 45° and 80° . We prefer a successive calculation of eight inversions for the subvertical initial orientations, that is for the inclination of 10° and the different azimuths, to just one inversion with a vertical initial orientation of the symmetry axis. The reason is that despite setting the initial inclination to 0° , the initial azimuth has to be defined as well and its value affects the solution. The initial strength of anisotropy is always 0.1 per cent, the initial 1-D

reference isotropic-velocity model is IASP'91 (Kennett & Engdahl 1991) and all the inversions consist of three iterations. After the calculations, we average the solutions of the eight inversions with a subvertical initial orientation of the axis. Then, we combine the 16 + 1 individual solutions at every parametrization node to obtain the final model, which maps the relatively high- and low-velocity directions of the parametrization cells.

The isotropic part of the final model is evaluated at each node as an average of the velocity perturbations resulting from the series of anisotropic inversions and it is displayed as a background, for example in Figs 6 and 7. Visualization of the anisotropic part of the solution, that is strength of anisotropy together with orientation of the symmetry axis, is more complicated. We either show all the 17 individual solutions for each node (left column in Figs 5c and d), or we calculate directional distribution of relatively high and low velocities by averaging the 17 individual solutions (right column in Figs 5c and d).

3.4 Directional analysis of relative *P*-wave traveltimes residuals

The main goal of this paper is to apply AniTomo to real data and to compare the results with independently derived velocity structure of the upper mantle. Plomerová *et al.* (2011) modelled the path-integrated anisotropic structure of the mantle lithosphere of northern Fennoscandia from the LAPNET data. We have reprocessed the LAPNET data set, extended it to the west, and complemented it in the north (Section 2). We evaluate the *P*-residual spheres showing the directional terms of the relative *P*-wave traveltimes residuals in the lower-hemisphere stereographic projection. The directional terms at a station express azimuth-incidence angle dependent parts of the relative residuals. We calculate the directional terms from the relative residuals by subtracting the station directional mean, which represents an average velocity beneath the station. To minimize effects of an uneven distribution of the events on the directional mean, we bin the relative residuals by azimuths and incidence angles. Distribution of the negative and positive terms in the *P* spheres, that is early and delayed wave arrivals relatively to a station average (directional mean), exhibits characteristic patterns, from which we can derive the low- and high-velocity directions beneath the stations. The *P*-sphere pattern allows us to derive path-integrated anisotropy beneath each station, while anisotropic tomography (AniTomo) retrieves anisotropy in the individual grid nodes. The stations with a similar pattern of the *P* spheres often cluster and delimit regions of a homogeneous anisotropy, related to large-scale tectonic units. For details of the method, we refer to, for example Babuška & Plomerová (1992, 2006). To verify results of the anisotropic tomography, we also calculate synthetic *P* spheres from synthetic traveltimes evaluated for the final anisotropic model retrieved by the coupled anisotropic-isotropic code.

4 RESULTS

4.1 Anisotropic tomographic model of the upper mantle beneath northern Fennoscandia

We present the final tomographic model of the anisotropic *P*-wave velocity of the upper mantle beneath northern Fennoscandia in two figures. Fig. 6 shows perturbations of the isotropic component of the anisotropic velocity (for simplicity referred further as velocity perturbations) at all depths and Fig. 7 shows the complete solution

of the anisotropic inversion at the 80, 120 and 170 km depth layers (see Fig. S4 for all the depth layers). We present the 3-D distribution of relatively high and low velocities averaged over all the individual solutions in each node (Fig. 7, on the left). The stereographic projection on the lower hemisphere makes possible to properly show the resulting 3-D distribution of relatively high- (blue) and low-velocity (red) directions at each grid node. The plots on the right (Fig. 7) show only regions of relatively uniform anisotropy and the characteristic *P*-sphere patterns. The whole set of the individual solutions is imaged in Fig. S4 on the left.

The shallowest layer of the model at the 20 km depth, where only isotropic-velocity perturbations are searched for, is characterized by a great variability of the velocity perturbations with amplitudes larger than 3 per cent (Fig. 6). The crust, of course, cannot be resolved well by the teleseismic tomography, but this layer absorbs heterogeneities of the thick Fennoscandian crust that are not completely compensated by the model of Moho depths used for *a priori* corrections of the travel times (Section 2). When we fix the 20 km depth and run the inversion from 50 km depth (not presented in this paper), the highly variable distribution of the isotropic-velocity perturbations occurs at the 50 km depth. The perturbations at the 50 km depth are similar to those imaged in the 20 km depth when the inversion at 20 km is allowed. This implies that allowing the inversion only from 50 km downward, the perturbations from the shallower crust are mapped into the 50 km depth of the model. When the isotropic-velocity inversion is allowed already at 20 km depth, the amplitudes of the velocity perturbations decrease at the 50 km depth to about 1 per cent, confirming thus separation of the remaining uncorrected crustal structures from the upper mantle. The two models (isotropic inversion allowed at 20 km and no inversion at 20 km) do not differ in the upper mantle from depth of 80 km downwards. At depths of 80 and 120 km, the amplitudes increase to 2 per cent. The strength of anisotropy reaches more than 3 per cent on average per layer down to 170 km. The layers at 80 and 120 km exhibit the strongest anisotropy that can be found in the model (Figs 7 and S4).

The mantle layers at depths of 80–170 km permit a detailed exploration of the results of the anisotropic inversion (Figs 6 and 7), which allows us to delimit regions of consistent anisotropy. For easier orientation, we mark these regions in each layer with numbers I–VI. Negative velocity perturbations of –2 per cent prevail in the western part of these depth layers and they shift towards the west with increasing depth. Strength of anisotropy is 3–4 per cent there and, particularly at depths of 120 and 170 km (Region III), directions of the relatively low velocities dip to the west or northwest, in general. The relatively high velocities lie approximately in a plane steeply dipping to the east or southeast. A sudden change of the anisotropic parameters sharply delimits the eastern boundary of the western region. Region III seems to be split into two subregions at a depth of 120 km by a zone of weaker anisotropy and velocity perturbations (hatched area in Figs 6, 7, S4 and S5). The part of Region III located eastward of this zone might be related to Region IV, delimited at the 80 km depth (Fig. 7a), in which the high-velocity directions dipping to the northeast prevail.

The northeastern part of the volume exhibits a laterally uniform, but depth dependent anisotropy with strength of about 3 per cent (Regions I and II, marked with orange in Figs 7 and S4). At the 50 and 80 km depths, the directions of relatively high velocities tend to dip to the north and the directions of relatively low velocities are perpendicular (Region I), while the anisotropic pattern is different at the 120 and 170 km depths. The directions of relatively low velocities dip to the northeast and the directions of relatively

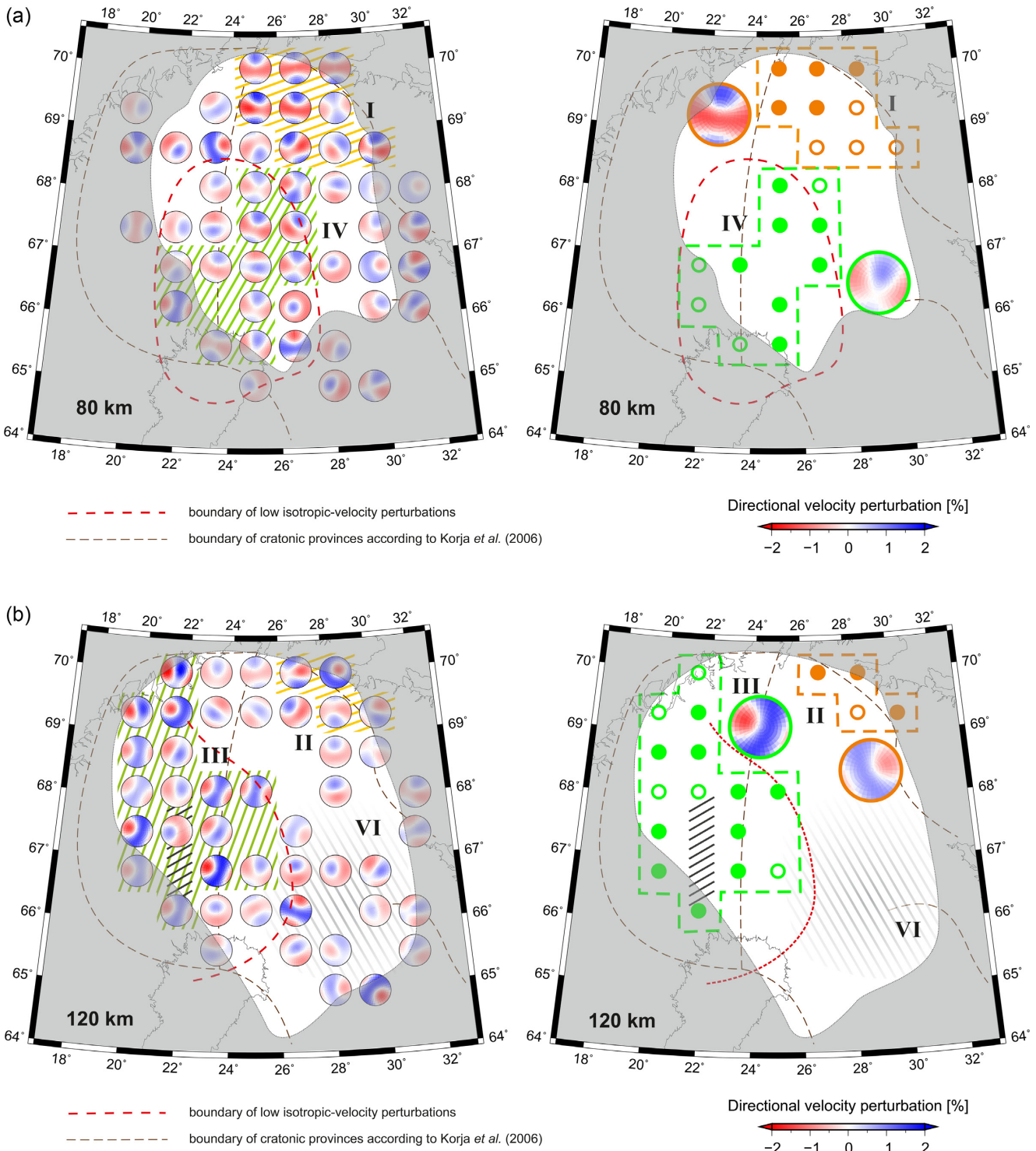


Figure 7. Anisotropic component of P -wave velocities at three selected depth layers (see Fig. S4 for all the depth layers). For each grid node we present the anisotropic velocities averaged from the set of individual solutions (left, see Fig. 5 for details). The anisotropic models are shown only for those nodes, for which at least eight individual solutions exhibit strength of anisotropy larger than 1 per cent. Nodes with a similar anisotropic pattern are marked as Regions I–V. A large region with no anisotropy at depth of 120 km is marked as Region VI. The black hatched area locates a zone of weaker anisotropy and velocity perturbations within Region III at depth of 120 km. The typical anisotropic patterns for Regions I–V are shown on the right (see Fig. 5 for details on visualization). Full circles mark nodes, in which the anisotropic pattern matches the typical pattern, while the empty circles mark nodes with only a tendency to the typical pattern. Red dashed curve contours the region with relatively low isotropic-velocity perturbations dominating the model. Part of the model with $RDE < 0.5$ is shaded. The brown dashed curves show boundaries of cratonic provinces after Korja *et al.* (2006); see also Fig. 1.

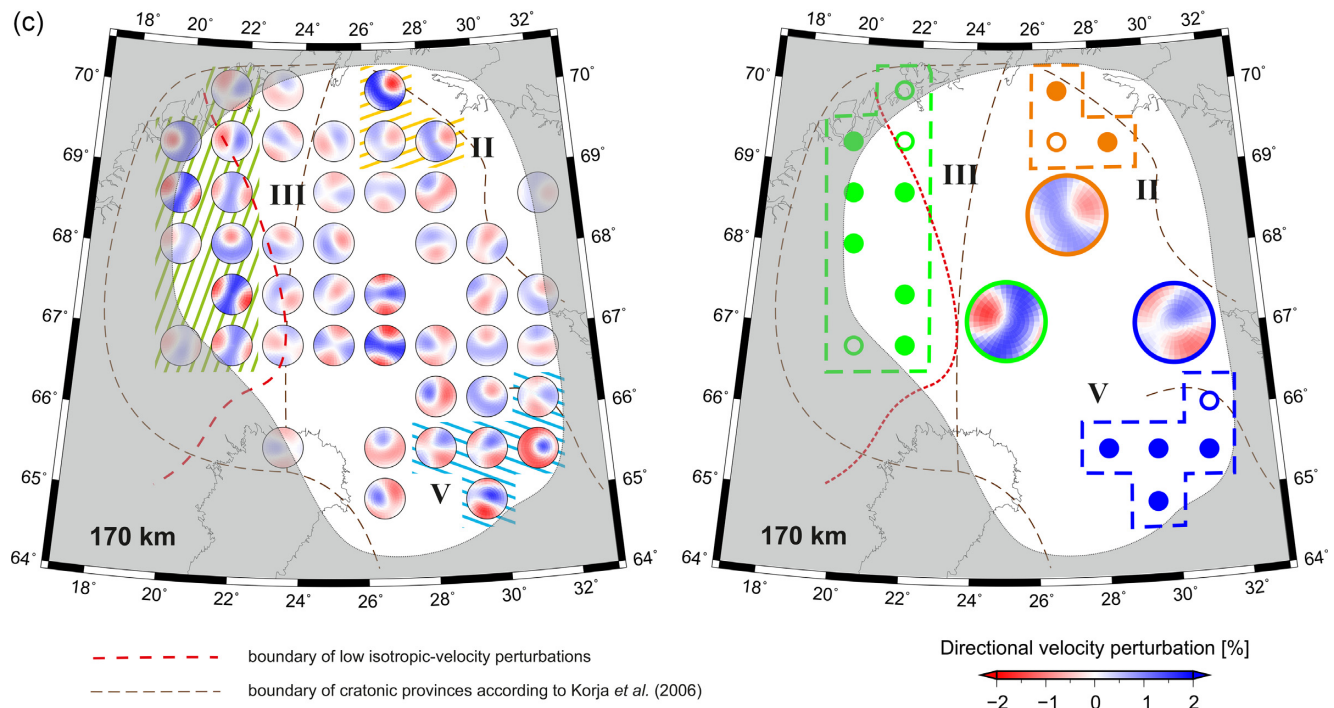


Figure 7. Continued.

high-velocities prevail in a plane dipping to the southwest (Region II).

The very southeastern part of the 170 km depth layer shows positive-velocity perturbations and directions of relatively high velocity dipping towards the northeast (Region V; marked with blue in Figs 7 and S4). The anisotropy retrieved in Region V coincides well with the path-integrated pattern of anisotropy modelled by Plomerová *et al.* (2006, 2011) and it will be discussed later. It is difficult to judge about anisotropy of Region V in shallower depths, where the parameters are not resolved reliably.

The model contains also zones of mostly weak and variable anisotropy among the regions with a consistent anisotropy (e.g. Region VI in Fig. 7b). Single-cell anisotropic patterns occur in these zones. A fragmented anisotropic pattern prevails at the 220 and 270 km depths (Fig. S4). The velocity perturbations below 1 per cent prevail at the depths from 220 km down to 370 km (Fig. 6).

Regarding a consistency among the models of the velocity perturbations coming out from the set of 24 anisotropic inversions, their standard deviation is lower than 1 per cent at all the grid nodes and it is even lower than 0.5 per cent in majority of the nodes (Fig. S6). Such a variation of the individual solutions is reasonably low in terms of teleseismic traveltimes tomography and it implies robustness of the average values as well (e.g. Fig. 6). Standard deviations of the velocity perturbations for the LAPNET data set are comparable with those resulting from various synthetic inversions presented in Section 4.2. Focusing on the anisotropic part of the model (the strength of anisotropy and orientation of the high- and low-velocity directions), one can see that the distribution of the individual solutions creates a systematic pattern at each grid node (Fig. S4 on the left). This confirms that the task is well determined and the solution is stable.

To support the results of the anisotropic inversion we compare images of the velocity perturbations from the set of anisotropic inversions (Fig. 6) with those from the purely isotropic inversion (Fig. S5). Distributions of velocity perturbations from both types

of the inversion are almost the same. The only difference is that the amplitudes of the velocity perturbations from the isotropic inversion are larger by about 0.2 per cent, on average, than those from the anisotropic inversions, indicating some leakage of velocity perturbations due to the neglected anisotropy in the isotropic images. The leakage is, however, very low and within the resolution limits of the teleseismic tomography, in which steep rays prevail. The resemblance of the velocity perturbations resulting from the purely isotropic inversion and the isotropic part of the anisotropic-velocity model confirms the reliable separation of the isotropic and anisotropic components of the final model.

Reduction of data variance, that is (initial variance—final variance)/initial variance, is 60 per cent for the isotropic-velocity inversion. Evaluation of variance reduction for the coupled anisotropic-isotropic inversion (Figs 7 and S4) is not as straightforward as in the isotropic case, because we can calculate this measure just for each inversion of the set of anisotropic inversions. For the individual anisotropic inversions, the data variance reduction attains values from 61 to 67 per cent, which is not a significantly better fit to the P -wave data compared to the fit of the purely isotropic inversion. Nevertheless, the solutions of the individual anisotropic inversions are affected by the initial orientation of the symmetry axis (Section 3.3) and thus, the fit of a single solution cannot be indeed a representative for the whole coupled anisotropic—isotropic model (Figs 6, 7 and S4). Note that the comparison of absolute RMS or variance reduction is a poor measure of the quality of the anisotropic results since the two inverse problems (purely isotropic and anisotropic) are significantly and systematically different. By principle it remains unclear how much of the purely isotropic solution is due to leakage from the ignored anisotropy and for the fully anisotropic solution it needs to be tested how well the parameter separation is working. In our case, the synthetic tests (see also Munzarová *et al.* 2018, and Section 4.2) showed that the coupled inversion of purely isotropic input does not create any artificial anisotropy.

4.2 Synthetic tests

We have designed various synthetic tests to explore capabilities of the LAPNET station-event distribution to resolve laterally and vertically variable heterogeneous anisotropic structure in the upper mantle, sharpness of boundaries, smearing of the input structures and, of course, a trade-off between anisotropy and lateral variations of isotropic velocity. The first synthetic model consists of three blocks with different isotropic components of velocity and anisotropy at depths of 80, 120 and 170 km to mimic a domain-like anisotropic structure in the mantle lithosphere (Figs 8 and S7). One of the blocks is purely isotropic, while the other two exhibit 5 per cent anisotropy with different orientations of the symmetry axes. Amplitude of the velocity perturbations is 3 per cent. We calculate traveltimes residuals of P waves propagating through the input model with respect to the IASP'91 reference model, considering the ray geometry of the LAPNET data set. Gaussian errors with standard deviation of 0.05 s are added to the calculated traveltimes mimicking the observation errors. For all synthetic tests, the inversion setup and setting of the control parameters is the same as for the inversion of the real data.

The block structure is qualitatively well recovered at the depths of 80, 120 and 170 km, where the synthetic input is assigned (Fig. S7). Nevertheless, the amplitudes of the velocity perturbations and the strength of anisotropy are underestimated at these depths in the retrieved model. The structure is smeared along the ray paths and it leaks to the shallower and deeper parts of the model, which is a typical drawback of any teleseismic tomography. Although the input parameters are homogeneous within each block, the output model parameters tend to vary among the individual nodes, but they correctly capture the general characteristics of the velocity perturbations and the relatively high- or low-velocity directions.

Fig. S8 presents resulting models at the 120 km depth for a set of synthetic tests that always follow the three-block structure (see Fig. S7), but with different isotropic components, as well as with different anisotropic parameters within the blocks. Despite various isotropic and anisotropic velocities of the individual blocks, sharp vertical boundaries between the blocks are well recovered. If the input is purely isotropic (Fig. S8c), no significant artificial anisotropy is generated in the output model. Similarly for the purely anisotropic input structures (Figs S8d–f), false weak velocity perturbations of only ~ 1 per cent could appear. The synthetic test in S8f documents that a similarity between an orientation of dominating ray path directions and an orientation of the symmetry axes of anisotropy can create false velocity heterogeneities. This is the case of the northeastern block, where the high-velocity directions dip towards the northeast, that is the azimuths, from which more waves arrive to the northeastern block compared to other azimuths. On the other hand, this is not the case of the northwestern block in the test in Fig. S8e.

We can find an effect similar to the generally observed feature called ‘overswinging’ of velocity perturbations around strong heterogeneities in the isotropic teleseismic tomography also for the anisotropic parameters in the anisotropic inversion. For example, in the northeastern block, where no anisotropy is prescribed (e.g. Figs S8a and b), a weak false anisotropy is created along the boundary with the other blocks. This effect accentuates the existence of a boundary by enhancing the contrast between the different parameters of the neighbouring blocks. The false anisotropy generated in the northeastern block tends to have a reversed distribution of the relatively high and low velocities compared with the anisotropy in the other blocks. The tests with an idealistic synthetic station-event

configuration (Munzarová *et al.* 2018) have also shown that localized artefacts with a size of a few cells may appear close to any boundary, that is either boundaries between heterogeneities within the model or close to the edges of the model itself, including the topmost and the deepest layers, where the inversion for anisotropy is allowed. Thus for the purposes of interpretation of the resulting anisotropic parameters, we consider only distinct signatures consistent over relatively large regions.

4.3 Clustering of path-integrated anisotropy according to P spheres

To further complement the information about the large-scale anisotropy of the upper mantle in northern Fennoscandia, we analyse the P -residual spheres (Section 3.4) calculated from the final anisotropic tomography model (synthetic spheres) and compare them with the spheres derived directly from the observed residuals (observed spheres).

Fig. 9 presents the observed P spheres clustered into several regions according to their pattern (see Fig. S9 for P spheres at individual stations). The regions exhibit uniform path-integrated anisotropy, in general. The pattern at stations in the northeast (Domains 1 and 2), in the west (Domain 3) and in the southern part (Domain 4) exhibit bipolar P -sphere patterns, which mean that the negative and positive directional terms concentrate in the complementary halves of the sphere. Such a pattern of the P spheres indicates that the observed anisotropic signal can be explained by anisotropy with plunging symmetry axes. On the contrary, the majority of the stations in the southeast do not show any systematic distribution of the relatively early and delayed arrivals. An exception is P -sphere pattern of stations MSF and KU6 at the very edge of the array (Domain 5). This pattern is in agreement with the P -sphere pattern observed at the stations deployed south of the LAPNET array during passive seismic experiment SVEKALAPKO (Plomerová *et al.* 2006, 2011). The division into regions is the same as in Plomerová *et al.* (2011), but the extent of Domain 3 in the northwest is larger due to complementing the data set.

The synthetic P spheres (Fig. 10) are evaluated from synthetic traveltimes of P waves propagating through the anisotropic part of the final model (on the right in Fig. S4). Comparison of the synthetic and the observed P spheres shows a large similarity as to their pattern and geographic distribution. On the other hand, absolute values of the synthetic directional terms are generally lower than those of the observed directional terms due to the probable underestimation of the strength of anisotropy in the averaged anisotropic model.

The synthetic P spheres at most of the stations located in the west (e.g. station MAS in Fig. 10) fit the pattern of Domain 3, in which the relatively early arrivals for the waves coming from the east dominate. The synthetic patterns are less distinctive than the observed patterns towards the southwest. Domain 1 and Domain 2, identified in the northeast of the array and characterized by relatively delayed arrivals of the waves coming from the east, are also reproduced very well by the synthetics as to their extent and the observed pattern (e.g. stations LP83 and LP65 in Fig. 10). Domain 4, located in the southern part of the array and characterized by relatively early arrivals of the waves coming from the northeast, can be clearly recognized in the synthetics as well (e.g. station LP41 in Fig. 10). The pattern of Domain 5, however, is only partly reproduced in the synthetic P spheres, because the domain is at the very edge of the array. Similarly to the observed P spheres, no pattern

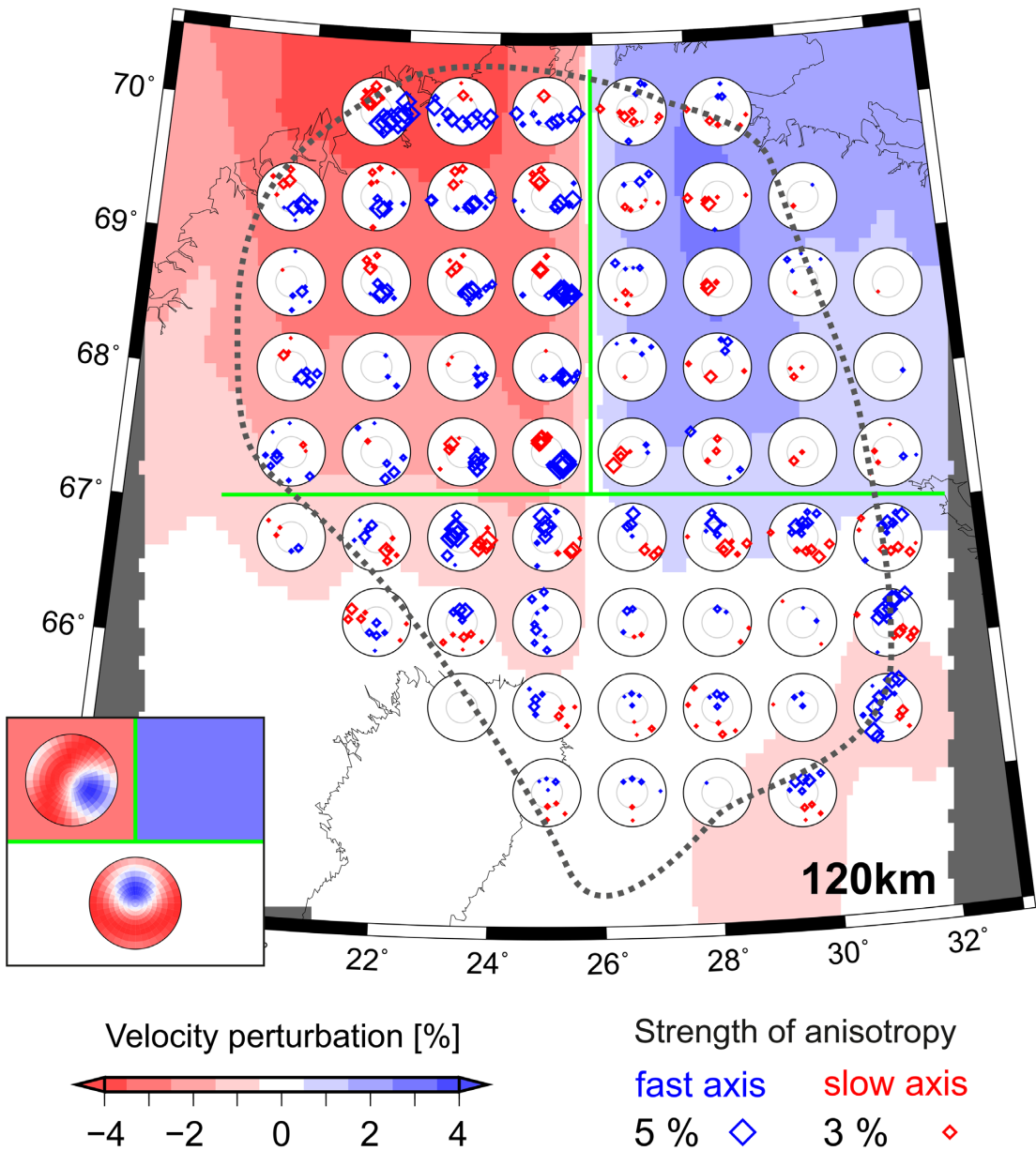


Figure 8. Anisotropic-velocity model at 120 km depth from the synthetic test mimicking a realistic anisotropic structure of the mantle lithosphere (results for all the depth layers are in Fig. S7). The synthetic model consists of three blocks with different isotropic velocities and anisotropy introduced into depths of 80, 120 and 170 km (schematic inset in the lower left-hand corner). Both the northwestern low-velocity and the northeastern high-velocity blocks exhibit 3 per cent amplitude of the isotropic-velocity perturbations relative to the IASP'91 reference model. Strength of anisotropy in the northwestern and in the southern block is 5 per cent. See captions of Figs 7 and 5 for description of plotting the output anisotropic parameters. Dotted black curve marks smoothed contour of RDE equal to 0.5.

prevails in the synthetic P spheres in the southeast, where the pattern is indistinctive and laterally variable.

5 DISCUSSION

5.1 Comparison of the anisotropic tomography model with independent inferences on anisotropy in the upper mantle

The AniTomo code is applied for the first time in the region, where anisotropy of the upper mantle has been studied also by different

methods. Therefore, we can validate the results of the unique approach of the coupled anisotropic–isotropic tomography with previous results.

Results presented in Section 4 demonstrate the high-degree compatibility between the observed and synthetic P spheres, showing the path-integrated anisotropy. The clustering of the two types of P spheres according to their patterns is almost identical (Fig. 10), though we compare results from a single-station method, which does not suffer from effects due to model edges, with results from the 3-D anisotropic tomography, in which resolution decreases towards model edges. Moreover, the single-station method, though with limited vertical resolution, is not limited by the grid spacing,

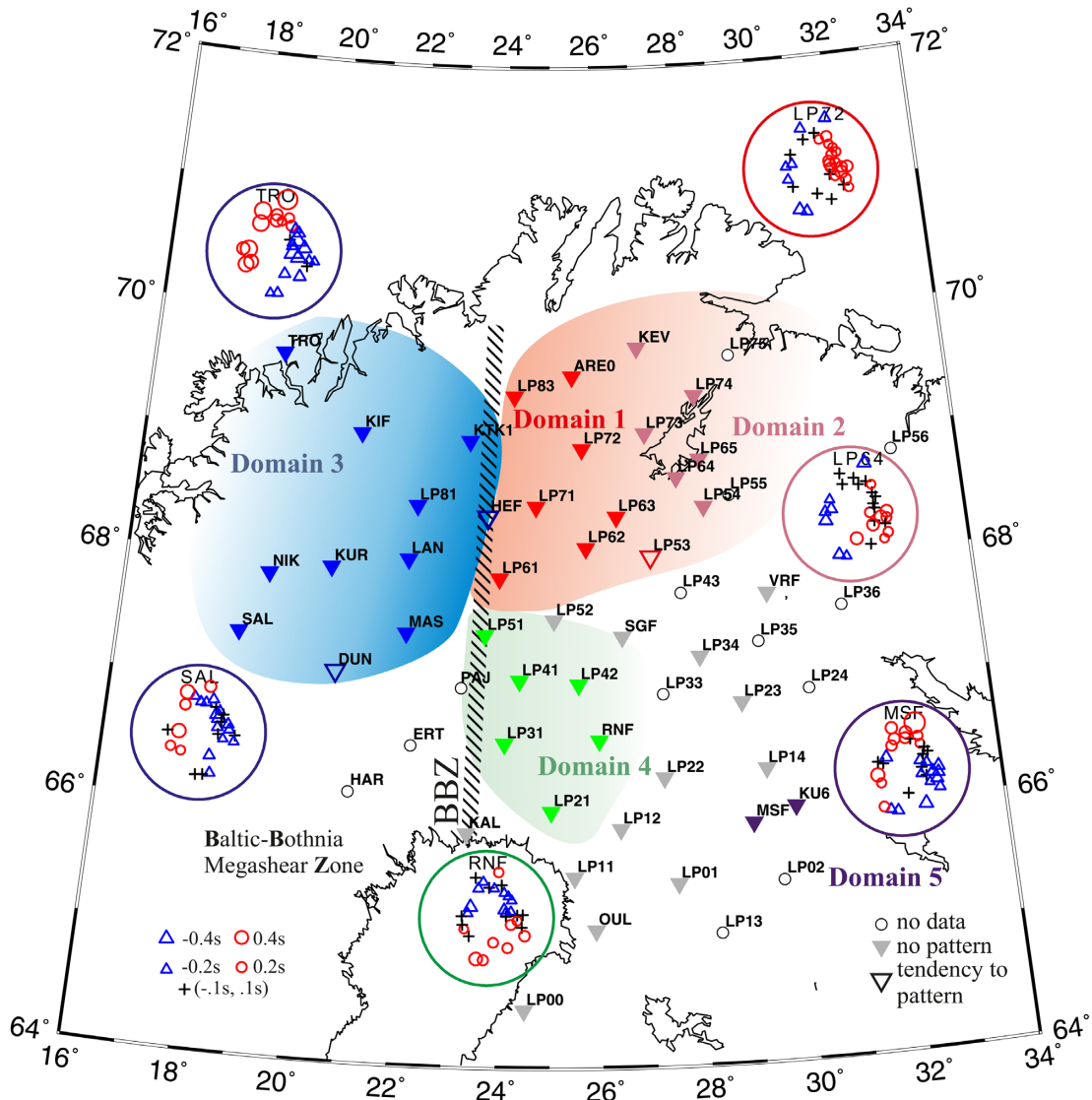


Figure 9. The mantle–lithosphere domains of northern Fennoscandia delimited according to similarity of directional distribution of relatively early and delayed P -wave arrival times at the individual stations of the extended LAPNET array (see fig. 2 by Plomerová *et al.* 2011, for the original LAPNET array). Each domain is characterized by a typical P sphere showing directional terms of the relative P -wave traveltimes residuals visualized in the lower-hemisphere stereographic projection. The P spheres cover incidence angles from 0° to 50° . Four domains with a distinct bipolar pattern in the west (Domain 3), northeast (Domains 1 and 2) and south (Domain 4) are delimited within the region studied. No distinct P -sphere pattern prevails in the southeast, except for the MSF and KU6 stations at the very edge of the array (Domain 5). See Fig. S9 for all the individual observed P spheres.

which is in our case 70 km by 70 km, and thus can detect lateral changes on a shorter scale.

Characteristics of the regions with a relatively uniform anisotropy that can be delimited in our tomographic model are compared in Tab. 1 with inferences on the path-integrated anisotropy modelled for individual domains of the mantle lithosphere by inversion of body-wave anisotropic parameters by Plomerová *et al.* (2011) and Vecsey *et al.* (2007). Distribution of the regions with a consistent anisotropy within the mantle lithosphere coming from both methods is in accord, in general, but, the tomographic model provides on top of that a vertical resolution.

Completely independent, though path-integrated as well, information on anisotropic structure of the upper mantle comes from the shear-wave splitting. Therefore, we superimpose the polarization azimuths of the fast split SKS waves (Plomerová *et al.* 2011) on dip directions of the high-velocity lineation or strikes of the

dipping high-velocity foliations retrieved within Regions I–V of our final P -wave anisotropic velocity model (Fig. 11). In the case of plunging symmetry axis b , the fast S polarizations vary around the strike of the dipping foliation plane in dependence on the back-azimuth. This leads to a seeming discrepancy between the average fast shear-wave polarization and the dipping high-velocity directions from the P -wave anisotropy, especially when the average fast S polarizations are associated with the fast velocity directions (see also Plomerová *et al.* 2011). On the other hand, in case of the models with dipping lineation, the fast S polarization azimuth and the azimuth of dipping high-velocities from P -wave anisotropy coincide. Despite the different wavelengths of the P and SKS waves analysed, the high-velocity directions of anisotropy of Regions I–V retrieved by the tomography and the fast-polarization azimuths correlate (Fig. 11). At nodes, where we show strikes of the dipping foliations of anisotropy retrieved by the coupled tomography, the

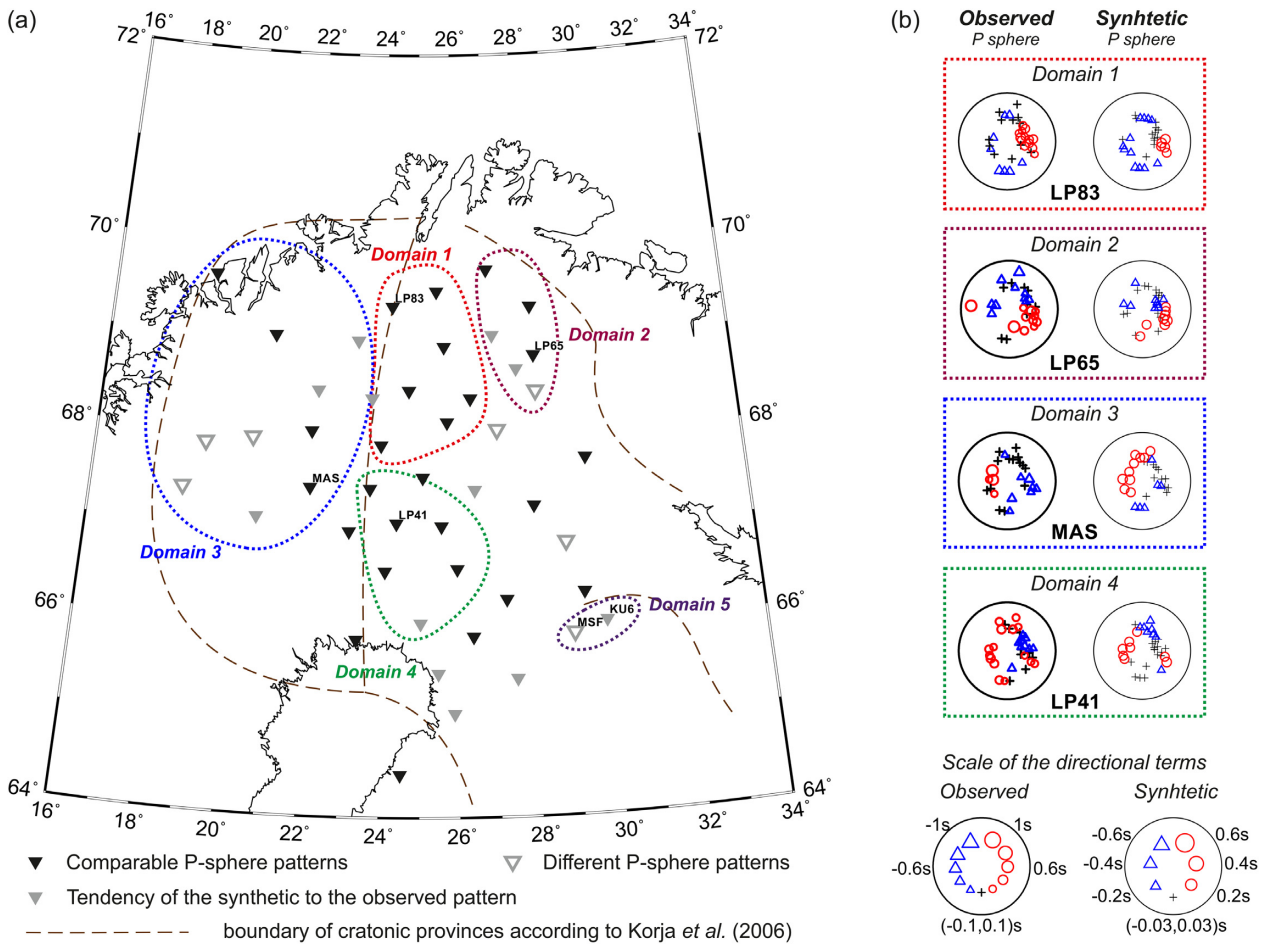


Figure 10. (a) Comparison of the observed P spheres (Fig. 9) and those calculated for the anisotropic model from the coupled anisotropic–isotropic tomography (Figs 7 and S4). Dotted curves group stations with a similar observed P -sphere pattern. (b) Examples of the synthetic and the observed P spheres for Domains 1–4. Stations with a sparse directional distribution of the rays are not considered in the analysis. For details about visualization of directional terms at a station, see caption of Fig. 9.

Table 1. Anisotropic characteristics of regions (left) and domains (right) in the upper mantle beneath northern Fennoscandia resulting from anisotropic tomography (this study, see also Fig. R2) and from a single-station study of path-integrated anisotropy (Plomerová *et al.* 2011).

Anisotropy from P -wave tomography (this study)					Path-integrated anisotropy from body-waves (Plomerová <i>et al.</i> 2011)					
Region	Axis	θ (°)	λ (°)	Depth (km)	Domain	Axis	P		$P + SKS$	
							θ (°)	λ (°)	θ (°)	λ (°)
I	<i>a</i>	80	0	50, 80	1	<i>b</i>	25	80	80	80
II	<i>b</i>	60	70	120, 170	2	<i>b</i>	30	105	80	105
III	<i>b</i>	60	300	120, 170	3	<i>b</i>	60	275	60	280
IV	<i>a</i>	60	30	80, (120)	4	<i>a</i>	15	55	70	55
V	<i>a</i>	60	40	170	*	<i>a</i>	70	60	60	30
VI	no consistent anisotropy				5	no P pattern, but SKS splitting				

*NW Archean (Vecsey *et al.* 2007).

Angles θ and λ represent inclination (measured from vertical) and, azimuth (measured clockwise from the north) of the hexagonal-symmetry axis.

azimuth of the fast S polarizations (evaluated in 3-D) vary along the strikes (e.g. the western part of the region). Whereas, in the northeast, where models with the a -axes prevail, the fast S polarization azimuths parallel the azimuth of dipping lineation.

Similarly to, for example Plomerová *et al.* (2006, 2011, 2012), Eken *et al.* (2010) and Munzarová *et al.* (2013), we relate the regional variations of the anisotropic velocity structure from the coupled tomography to domains of the mantle lithosphere preserving the fossil fabrics, because at depths below the lithosphere bottom

the anisotropy is weak in general. The only discrepancy between the single station analysis of path-integrated anisotropic characteristics of P and S waves was detected in the southeastern part of the LAPNET array (Plomerová *et al.* 2011), in which P waves do not detect any anisotropy (no P pattern; see Figs 9 and S9), whereas the shear waves show significant splitting (see, e.g. Fig. 11). Though the final tomographic model (Fig. S4) shows only very weak and variable anisotropy at depth of 220 km and deeper in general, it localizes some anisotropy at depth of 270 km around 67°–68°N and

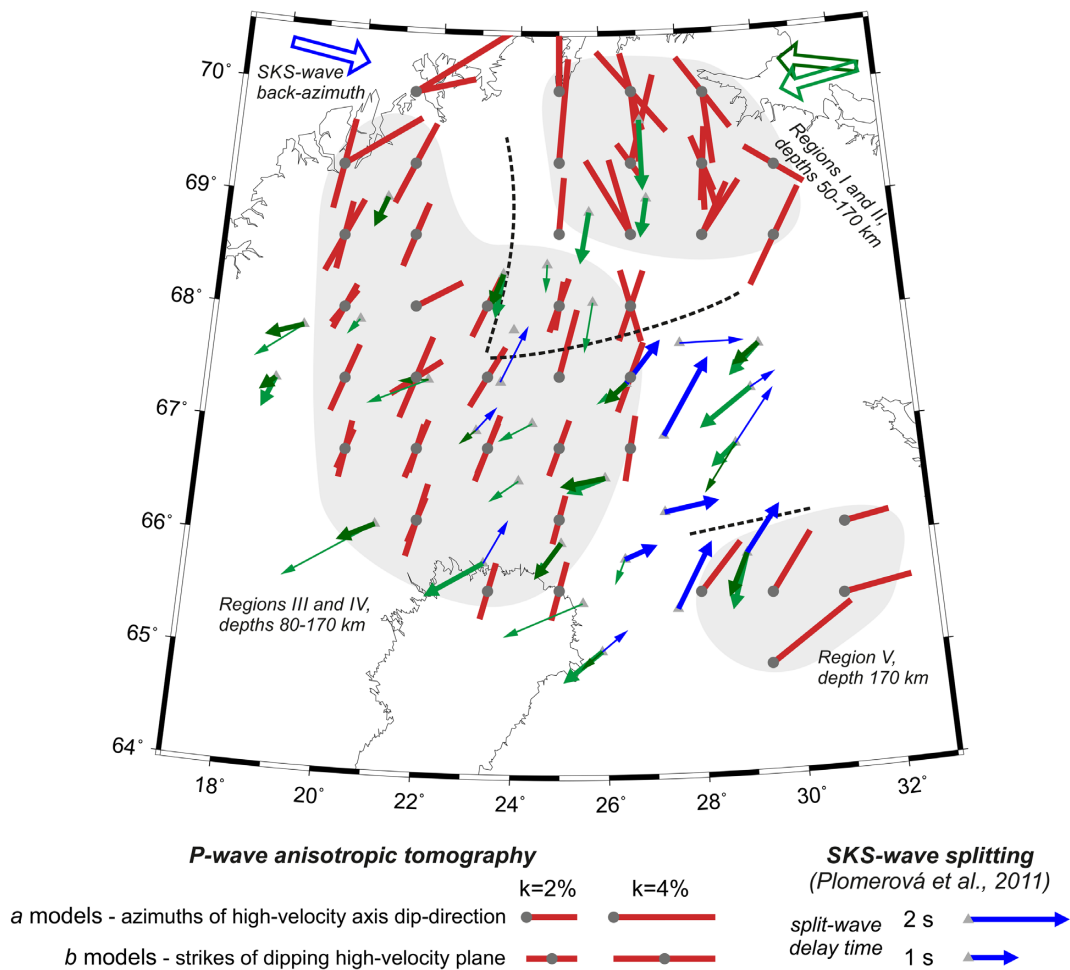


Figure 11. Polarization azimuths of the fast split shear waves evaluated at the LAPNET stations for three teleseismic events (Plomerová et al. 2011) plotted together with the azimuths of dip directions of the high-velocity *a*-axis models or the azimuth of strikes of the dipping high-velocity plane for the *b* models resulting from the *P*-wave coupled anisotropic-isotropic velocity tomography. We plot the anisotropy from the tomography only for Regions I–V jointly for all the depth layers of the model where those regions are located (grey background delimits Regions I–V; see Figs 7 and S4). The line segments representing the *a*-axis azimuths start in the parametrization nodes (coloured crosses), while the line segments marking the strikes of dipping (*a,c*) foliations are centred in the corresponding nodes. Good and firm splitting measurements (thick and thin arrows, respectively) and domain boundaries (black dashed curves) according to Plomerová et al. (2011). The azimuths of the fast *S* polarizations (evaluated in 3-D) vary along the strikes of the dipping foliations retrieved by the tomography, or, parallel the dipping lineation and document thus compatibility of the two independent inferences on the upper mantle anisotropy.

26°–29°E (Fig. S4). This region of deep anisotropy correlates with the area of large split delay times and does not have any anisotropic equivalent in the *P* spheres.

5.2 Comparison of velocity perturbations from anisotropic and isotropic tomography models

For simplicity of the discussion, we denote *P*-wave velocity perturbations retrieved by the coupled anisotropic-isotropic inversion with AniTomo as Model 1 (Fig. 6), those from purely isotropic inversion by AniTomo as Model 2 (Fig. S5) and perturbations from isotropic inversion by Telinv as Model 3 (Silvennoinen et al. 2016). The recently published Model 3 for the upper mantle beneath northern Fennoscandia was calculated with standard isotropic inversion code Telinv (Section 3). Silvennoinen et al. (2016) evaluated the *P* wave traveltimes residuals for the LAPNET network independently. In the south of the region they complemented the data set with measurements from seismic array SVEKALAPKO (e.g. Sandoval et al. 2004; Hjelt et al. 2006). The velocity perturbations of anisotropic

Model 1 and isotropic Model 2, calculated with AniTomo, are almost identical as to distribution of relative perturbations. They both show similar gross features as the isotropic Model 3, particularly at depths of 120 and 170 km (180 km in Model 3 by Silvennoinen et al. 2016), where the relatively low-velocity heterogeneity dominates the well-resolved central part of the region. However, in Model 1 and Model 2, the low-velocity heterogeneity shifts towards the west with increasing depth, while in the isotropic Model 3, this heterogeneity splits and surrounds the central unperturbed part of the model.

Compared to anisotropic Model 1, higher amplitudes of the velocity perturbations prevail in the isotropic Model 3 (Silvennoinen et al. 2016). However, the amplitudes of the velocity perturbations resulting from teleseismic traveltimes tomography are very sensitive to a setup of the inversion (e.g. Foulger et al. 2013; Munzarová et al. 2018), for example damping factor of velocity perturbations. Model 3 is calculated with a relatively low damping factor and a higher number of iterations compared to the anisotropic Model 1, which both contribute to larger amplitudes of the resulting

velocity perturbations, in general. Lateral variations of the velocity perturbations in Model 1 and Model 2 considerably decrease with depth. At 220 km and deeper, they hardly exceed 2 per cent in the well-resolved parts. On the contrary, in the highly heterogeneous Model 3, the lateral variations of the velocity perturbations reach 7 per cent at almost all the parametrization layers and they do not decrease with depth. It is a general characteristic of teleseismic tomography that unresolved parts of the residuals are mapped into the deepest parts of the models.

Reversed positive and negative perturbations at 80 km depth result from differences in the model parametrizations at shallower depths. The 80 km depth is the first layer, at which the velocity perturbations are searched in Model 3, while in Model 1 and Model 2 we start inverting for velocity at 20 and 50 km depths to accommodate crustal structures uncompensated by the *a priori* assumed model of the Moho (Silvennoinen et al. 2014). Therefore, the first layers in Model 1 or Model 2, that is 20 km (Figs 6 and S5), and 80 km in Model 3, resemble each other. The 80 km depth of Model 3 might be biased by the leakage of the shallow structures into greater depths (Karousová et al. 2012).

5.3 Trade-off between anisotropy and lateral variations of isotropic velocity

The anisotropic tomographic inversion of P -wave traveltimes residuals, performed by novel code AniTomo, is a unique approach to study heterogeneous anisotropic structure of the upper mantle. Our work covers also investigation of a potential trade-off between anisotropy and spatial variations of isotropic velocity, which might play a significant role not only in the coupled anisotropic–isotropic tomography, but also in the standard approach of isotropic interpretation of seismic-wave traveltimes. We have performed a large series of synthetic tests of the new code, showing that for a quasi-even realistic distribution of stations and teleseismic events, the upper-mantle anisotropy can be sufficiently separated from lateral variations of the isotropic velocities by the simultaneous inversion (Munzarová et al. 2018).

Regarding the LAPNET data set, exhibiting, as any real data set, an unequal distribution of rays, we have carefully studied the resolution capability of its station-event configuration before the inversion. Based on analysis of the ray density tensors (Section 3.2), we allow the fully anisotropic inversion only in a limited volume within the depths layers from 50 km down to 270 km (Fig. 3). Results of the inversions with different settings, that is from purely isotropic to anisotropic ones, the second one with various initial orientations of the symmetry axis, exhibit a stable consistency among the individual anisotropic solutions and a very low variability of the velocity perturbations (Section 4.1).

The results of the extensive series of synthetic tests (Section 4.2) demonstrate that the inversion setup together with the LAPNET ray geometry can detect anisotropic structures of the upper mantle with a limited trade-off between isotropy and anisotropy. Boundaries between various synthetic blocks are recovered reliably in the output models, confirming thus plausibility of, for example westward inclination of the eastern boundary of Region III (Fig. 7). On the other hand, we cannot avoid some undesirable effects that are typical of teleseismic tomography, such as underestimated output amplitudes or vertical smearing of the structures. The resulting amplitudes of the velocity perturbations (up to 2 per cent at 80 and 120 km depths) and the strength of anisotropy (up to 3–4 per cent at 80 and 120 km depths) of the final tomographic model might be considered as the

lower limit of the real parameters. We would like to note that the synthetic tests presented in this publication are focused particularly on the mantle lithosphere and the upper mantle beneath relatively stable continental regions without extremal heterogeneities in the mantle, for example subduction zones. The main target of this study is the application of the novel coupled tomography on real data and therefore, we chose Fennoscandia as a representative of such a region. For studies of active regions, for example active subduction zones, which include strongly variable heterogeneities and complex anisotropy in the asthenosphere, further testing of new code AniTomo would be appropriate.

5.4 LAB in northern Fennoscandia

The lithosphere–asthenosphere boundary (LAB) in northern Fennoscandia is modelled mostly at depths of \sim 150 km by applying different techniques with the use of the LAPNET array data (Plomerová & Babuška 2010; Pedersen et al. 2013; Vinnik et al. 2014). The LAB deepens towards southcentral Finland, where the Karelian craton root extends below 200 km (Artemieva 2006; Plomerová et al. 2008). Pedersen et al. (2013) reveal a decrease of S -wave velocity at 150 km depth by inverting the dispersion curve of Rayleigh waves recorded during the LAPNET experiment. Vinnik et al. (2016) estimate the depth of LAB at 160 km by analysis of S receiver functions. All these results comply well with the decrease of variations of the isotropic velocities accompanied by reduction of the anisotropy at the depth layer of 220 km compared to the 170 km layer of our tomographic model. This can be related to a structural change from lithosphere to asthenosphere at depth around 170 km (Figs 6 and S4). To document that anisotropy potentially located below the 170 km depth can be, in principle, detected by our tomographic setup, we design a synthetic model with two anisotropic blocks lying one above the other (Fig. S10). The results of the synthetic test show that the tomographic inversion is able to resolve correctly a vertically variable anisotropic structure down to 220 km depth. However, if anisotropy with a subhorizontal preferred orientation of the symmetry axis prevails in the asthenosphere, which is modelled, for example by Vinnik et al. (2014), it might remain partly undetected by our tomographic inversion because of the limited range of angles of propagation of the teleseismic P waves from 20° to 50° .

5.5 The anisotropic tomographic model in light of tectonic settings

The results of anisotropic tomography of the upper mantle beneath northern Fennoscandia presented in this paper are in accord with the domain-like anisotropic structure of the mantle lithosphere inferred from path-integrated anisotropic parameters of P - and SKS-waves (Plomerová et al. 2011). The anisotropic tomography allows us to follow structural changes in the volume studied not only laterally, but also with depth. The lithosphere of northern Fennoscandia preserves fossil fabrics (e.g. Babuška et al. 1993; Plomerová & Babuška 2010) of Archean microplate nuclei assembled during Palaeoproterozoic orogenic processes (e.g. Lahtinen et al. 2005; Weiher et al. 2005; Korja et al. 2006). The individual microplate nuclei are separated by accreted mixtures of island arcs, terranes and mobile belts, such as Inari and Kittilä arcs or Belomorian mobile belt (see Fig. 1b).

In light of the large-scale tectonics, we associate western Region III marked in slices at depth 120 and 170 km (Fig. 7) mostly

with the mantle lithosphere of the Norrbotten craton, accreted to the Karelian and Kola provinces (Fig. 1b). Following the westward shift of the anisotropic pattern as well as the low-velocity perturbations with increasing depth (Figs 6 and 7), Region III seems to thrust over the provinces to the east (Fig. S11). The tomography images the Norrbotten craton down to ~ 170 km depth. The low-velocity perturbations within the Norrbotten mantle lithosphere were also modelled by teleseismic P -wave isotropic-velocity tomography of the upper mantle below the Swedish national seismological network by Eken *et al.* (2007) and in anisotropy-corrected tomography (Eken *et al.* 2012). The margins of the Norrbotten craton could have undergone modification during the accretion process, but the inherited pre-collisional fabric of the rigid mantle lithosphere survived. Anisotropy in this region is approximated by low-velocity axis b plunging towards northwest by both the coupled tomography as well as by inversion of the P - and SKS-wave anisotropic parameters (Domain 3 in Table 1; Plomerová *et al.* 2011).

The pattern characteristic for Region III at depth of 120 and 170 km diminishes at depth of 80 km, where we see Region IV above the southeastern part of Region III. It is approximated by anisotropy with the high-velocity symmetry a axis dipping towards the northeast (see also model of Domain 4, Table 1). At the 120 km depth, roughly along 22°E latitude, there is a zone of weaker anisotropy and velocity perturbations within Region III (hatched area in Figs 6, 7, S4 and S5). Admitting the existence of such a zone, the subregion located eastward might be related to a potential downward continuation of Region IV. Azimuths of the high-velocity directions due to the fabrics of Regions III and IV are close, though the models of anisotropy differ. The geographical location of the zone of weaker anisotropy roughly correlates with the Baltic-Bothnia megashear Zone at the surface (BBZ; Fig. 1b), a suture zone between the Norrbotten and Karelian cratons. Moreover, the fabric of Region IV, revealed in the coupled tomography, coincides with the fabric of the Karelian domain modelled from the SVEKALAPKO experiment data (Plomerová *et al.* 2006; Vecsey *et al.* 2007).

From the tectonic point of view, the eastern part of the target region is more complex. The complexity of the tomographic model in the northeast probably mirrors deep structure of the various accreted arcs mapped at the surface (Korja *et al.* 2006) and intervening the Kola and Norrbotten cratons (Fig. 1). The coupled tomography images two regions in the northeast. Region II located in the northeast at the 120 and 170 km depths is shifted by ~ 100 km northeastward with respect to Region I, which is delimited at the 50 and 80 km depths (Figs 7 and S4). Although we are discussing the very edge of the tomographic model, the results are supported by the path-integrated anisotropy modelled by Plomerová *et al.* (2011), who identified narrow Domain 1 and Domain 2 in the mantle lithosphere (see also Table 1). The anisotropy revealed in Region I differs, at first glance, from path-integrated anisotropy suggested for either Domain 1 or Domain 2 by Plomerová *et al.* (2011). A depth-variable anisotropy, which can be detected in the coupled tomography, can contribute to that. Nevertheless, the similarity of the synthetic and observed P spheres (Figs 10 and 11) documents that the 3-D distribution of anisotropy modelled by the coupled tomography in the upper mantle comply with the path-integrated P -sphere patterns evaluated for the individual stations.

Southward of the northeastern Region I and Region II, where the Belomorian mobile belt separates the Kola and Karelian cratons, no large-scale regionally consistent anisotropy appears in our tomographic model of P -wave anisotropic velocities. Similarly, no anisotropic signal is identified in the observed P -spheres (Fig. 9).

However, strong splitting of SKS waves was evaluated there (Plomerová *et al.* 2011). If none of the methods employing teleseismic P waves detects anisotropic signal, but shear waves split, then the symmetry axis is probably horizontal. Because dipping fabrics prevail in the continental domains of the mantle lithosphere investigated up to now (e.g. Babuška & Plomerová 2006; Plomerová *et al.* 2012), the anisotropic signal detected by the SKS waves probably originates at depths below ~ 250 km. These depths assign the anisotropy into the sublithospheric upper mantle, which allows us to relate the anisotropy to the present-day flow in the asthenosphere.

In the very southeastern margin of the model the tomography detects anisotropic signal yet at depth of 170 km. Keeping in mind that resolution of any tomography at its edges is low, we would not rely on the results. However, the anisotropic model with high-velocity a -axis plunging to the northeast is identical with the fabric derived from both the LAPNET and the SVEKALAPKO data for the Karelian lithosphere, whose thickness attains about 200–220 km in the southcentral Finland (Plomerová *et al.* 2006; Vecsey *et al.* 2007).

6 CONCLUSIONS

We present a tomographic model of coupled P -wave isotropic-velocity perturbations and velocity anisotropy of the upper mantle beneath northern Fennoscandia. The anisotropic tomography is based on our new code AniTomo (Munzarová *et al.* 2018) applied on 3286 relative traveltimes residuals of teleseismic P waves recorded during passive seismic experiment LAPNET. AniTomo is a novel and unique code considering weak anisotropy with symmetry axes oriented generally in 3-D, that is including axes inclination. The model parameters, iteratively searched at nodes of a 3-D parametrization grid, are perturbations of isotropic component of velocity, strength of anisotropy and orientation of the hexagonal-symmetry axis defined by an azimuth and inclination. After an extensive testing of the code on realistic synthetic data sets and structures (Munzarová *et al.* 2018), we apply the code (this issue) for the first time on a real data recorded in the Archean part of Fennoscandia. We carry out a careful analysis of the ray distribution and document ability of the code to resolve large-scale anisotropic structures in the upper mantle of Fennoscandia by a series of specifically designed synthetic tests.

Images of isotropic component of the anisotropic-velocity perturbations show gross features similar to images of velocity perturbations from the purely isotropic inversion. This means that for the setup of our inversions, there is only a small leakage of anisotropic perturbations into the isotropic model, when anisotropy is neglected. Thus, the isotropic and anisotropic parts of the model resulting from the anisotropic inversion are sufficiently separated.

The largest velocity perturbations and the strongest anisotropy concentrate at depth of 80–170 km, that is in the mantle lithosphere. Below these depths, the lateral velocity variations decrease significantly.

According to the modelled anisotropy, which varies both laterally and vertically, the mantle lithosphere of northern Fennoscandia can be divided into several regions exhibiting consistent fabrics. The delimited regions correlate with the tectonic units and their boundaries often correlate with prominent sutures in the crust. The Baltic-Bothnia megashear Zone, the most significant suture zone in the region, seems to have its imprint in the mantle–lithosphere as well.

We identify mantle lithosphere domain associated with the Norrbotten craton, characterized by a distinct anisotropy of about 3–4

per cent strength down to \sim 170 km depth. A relatively complex depth-varying anisotropy in the northeast of the model likely reflects deep structure of various arcs accreted in between the Kola and Norrbotten cratons. The southeastern part of the tomographic model shows a less consistent large-scale *P*-wave anisotropy. A small region in the very southeast margin exhibits a fabric similar not only to that revealed by single-station methods from the LAPNET data (Plomerová *et al.* 2011), but also to that in the Karelian mantle lithosphere from data of experiment SVEKALAPKO in southcentral Finland (Plomerová *et al.* 2006; Vecsey *et al.* 2007).

Anisotropic tomography retrieves individual regions characterized by consistent, but differently oriented fabrics. The regions are compatible with the domains delimited by joint studies of path-integrated anisotropy from directional analysis of *P*-wave travel-time residuals and SKS-wave splitting parameters (Plomerová *et al.* 2011). We relate the domain-like anisotropic structure to blocks of Archean mantle lithosphere, which probably preserve their original fossil fabrics. The fabrics mostly survived various tectonic events including the lithosphere domain accretion, as well as the Palaeoproterozoic orogenic processes when northern Fennoscandia was formed.

LAPNET WORKING GROUP

Elena Kozlovskaia¹, Helle Pedersen³, Jaroslava Plomerová⁶, Ulrich Achauer⁴, Eduard Kissling⁷, Irina Sanina⁸, Teppo Jämsen¹, Hanna Silvennoinen¹, Catherine Pequegnat³, Riitta Hurskainen¹, Robert Guiguet³, Helmut Hausmann⁵, Petr Jedlička⁶, Igor Alešhin¹⁰, Ekaterina Bourova³, Reynir Bodvarsson¹¹, Evald Brückl¹⁰, Tuna Eken⁶, Pekka Heikkinen², Gregory Houseman¹⁴, Helge Johnsen¹², Elena Kremenetskaya⁹, Kari Komminaho², Helena Munzarová¹², Roland Roberts¹¹, Bohuslav Růžek⁶, Hossein Shomali¹¹, Johannes Schweitzer¹³, Artem Shaumyan⁸, Luděk Vecsey⁶, Sergei Volosov⁸

Institutions participating in the creation of the data set

1. Sodankylä Geophysical Observatory of the University of Oulu, Finland
2. Institute of Seismology of the University of Helsinki, Finland
3. University of Grenoble, France
4. University of Strasbourg, France
5. Institute of Geodesy and Geophysics, Vienna University of Technology, Austria
6. Geophysical Institute of the Czech Academy of Sciences, Prague, Czech Republic
7. Institute of Geophysics ETH Zürich, Switzerland
8. Institute of Geospheres Dynamics of the Russian Academy of Sciences, Moscow, Russia
9. The Kola Regional Seismological Centre, of the Russian Academy of Sciences, Russia
10. Geophysical Centre of the Russian Academy of Sciences, Schmidt Institute of Physics of the Earth of the Russian Academy of Sciences, Russia
11. Swedish National Seismological Network, University of Uppsala, Sweden
12. Institute of Solid Earth Physics, University of Bergen, Norway
13. NORSTAR, Norway
14. University of Leeds, UK

ACKNOWLEDGEMENTS

The research was supported by grant no. 210/12/2381 of the Grant Agency of the Czech Republic and by project CzechGeo/EPOS-Sci,

no. CZ.02.1.01/0.0/0.0/16_013/0001800, financed from the Operational Programme Research, Development and Education within ERDF. We would like to thank to Dr Lapo Boschi for his editorial work and to two anonymous reviewers for their thorough reviews that helped to improve the manuscript. Contributions of all members of the LAPNET Working Group are greatly appreciated. Figures were plotted with the use of the Generic Mapping Tools (Wessel & Smith 1998).

REFERENCES

- Arlitt, R., Kissling, E. & Ansorge, J., 1999. Three-dimensional crustal structure beneath the TOR array and effects on teleseismic wavefronts, *Tectonophysics*, **314**, 309–319.
- Artemieva, I.M., 2006. Global $1^\circ \times 1^\circ$ thermal model TC1 for the continental lithosphere: implications for lithosphere secular evolution, *Tectonophysics*, **416**, 245–277.
- Auer, L., Boschi, L., Becker, T.W., Nissen-Meyer, T. & Giardini, D., 2014. Savani: a variable resolution whole-mantle model of anisotropic shear velocity variations based on multiple data sets, *J. geophys. Res.: Solid Earth*, **119**, 3006–3034.
- Babuška, V. & Cara, M., 1991. *Seismic Anisotropy in the Earth*, Kluwer Academic Publishers.
- Babuška, V. & Plomerová, J., 1992. The lithosphere in central Europe—seismological and petrological aspects, *Tectonophysics*, **207**, 141–163.
- Babuška, V. & Plomerová, J., 2006. European mantle lithosphere assembled from rigid microplates with inherited seismic anisotropy, *Phys. Earth. planet. Inter.*, **158**, 264–280.
- Babuška, V., Plomerová, J. & Šílený, J., 1993. Models of seismic anisotropy in the deep continental lithosphere, *Phys. Earth. planet. Inter.*, **78**, 167–191.
- Bezada, M.J., Faccenda, M. & Toomey, D.R., 2016. Representing anisotropic subduction zones with isotropic velocity models: a characterization of the problem and some steps on a possible path forward, *Geochim. Geophys. Geosyst.*, **17**, 3164–3189.
- Chang, S.J., Ferreira, A.M.G., Ritsema, J., van Heist, H.J. & Woodhouse, J.H., 2015. Joint inversion for global isotropic and radially anisotropic mantle structure including crustal thickness perturbations, *J. geophys. Res.*, **120**, 4278–4300.
- Chyba, J., Plomerová, J., Vecsey, L. & Munzarová, H., 2017. Tomography study of the upper mantle around the TESZ based on PASSEQ experiment data, *Phys. Earth planet. Inter.*, **266**, 29–38.
- Cooper, A.K., Barrett, P.J., Stagg, H., Storey, B., Stump, E. & Wise, W., the 10th ISAES editorial team, eds., 2008. Antarctica: a Keystone in a Changing World. *Proceedings of the 10th International Symposium on Antarctic Earth Sciences*, National Academic Press, Washington, DC.
- Debayle, E., Dubuffet, F. & Durand, S., 2016. An automatically updated S-wave model of the upper mantle and the depth extent of azimuthal anisotropy, *Geophys. Res. Lett.*, **43**(2), 674–682.
- Eken, T., Shomali, H., Roberts, R. & Bodvarsson, R., 2007. Upper mantle structure of the Baltic Shield below the Swedish National Seismological Network (SNSN) resolved by teleseismic tomography, *Geophys. J. Int.*, **169**, 617–630.
- Eken, T., Plomerová, J., Roberts, R., Vecsey, L., Babuška, V., Shomali, H. & Bodvarsson, R., 2010. Seismic anisotropy of the mantle lithosphere beneath the Swedish National Seismological Network (SNSN), *Tectonophysics*, **480**, 241–258.
- Eken, T., Plomerová, J., Vecsey, L., Babuška, V., Roberts, R., Shomali, H. & Bodvarsson, R., 2012. Effects of seismic anisotropy on P-velocity of the Baltic Shield, *Geophys. J. Int.*, **188**, 600–612.
- Fichtner, A., Kennett, B.L.N., Igel, H. & Bunge, H.P., 2010. Full waveform tomography for radially anisotropic structure: new insights into present and past states of the Australasian upper mantle, *Earth planet. Sci. Lett.*, **290**, 270–280.
- Fichtner, A., Saygin, E., Taymaz, T., Cupillard, P., Capdeville, Y. & Trampert, J., 2013. The deep structure of the North Anatolian fault zone, *Earth planet. Sci. Lett.*, **373**, 109–117.

- Fouch, M.J. & Rondenay, S., 2006. Seismic anisotropy beneath stable continental interiors, *Phys. Earth planet. Inter.*, **158**, 292–320.
- Foulger, G.R. *et al.*, 2013. Caveats on tomographic images, *Terra Nova*, **0**, 1–23.
- French, S.W. & Romanowicz, B.A., 2014. Whole-mantle radially anisotropic shear velocity structure from spectral-element waveform tomography, *Geophys. J. Int.*, **199**(3), 1303–1327.
- Hammond, W.C. & Toomey, D.R., 2003. Seismic velocity anisotropy and heterogeneity beneath the Mantle Electromagnetic and Tomography Experiment (MELT) region of the East Pacific Rise from analysis of P and S body waves, *J. geophys. Res.*, **108**(B4), 2176.
- Hirahara, K. & Ishikawa, Y., 1984. Travel time inversion for three-dimensional P-wave velocity anisotropy, *J. Phys. Earth*, **32**, 197–218.
- Hjelt, S.-E., Korja, T., Kozlovskaya, E., Lahti, I. & Yliniemi, J., & BEAR and SVEKALAPKO Working Groups, 2006. Electrical conductivity and seismic velocity structures of the lithosphere beneath the Fennoscandian Shield, in *European Lithosphere Dynamics*, Vol. **32**, pp. 541–559, eds Gee, D. & Stephenson, R., Geol. Soc. London, Mem. Ser.
- Ho, T., Priestley, K. & Debayle, E., 2016. A global horizontal shear velocity model of the upper mantle from multimode Love wave measurements, *Geophys. J. Int.*, **207**(1), 542–561.
- Hua, Y., Zhao, D. & Xu, Y., 2017. P wave anisotropic tomography of the Alps, *J. geophys. Res.: Solid Earth*, **122**, 4509–4528.
- Ishise, M. & Oda, H., 2005. Three-dimensional structure of P-wave anisotropy beneath the Tohoku district, northeast Japan, *J. geophys. Res.*, **110**, B07304.
- Karousová, H., Plomerová, J. & Babuška, V., 2012. A three-dimensional velocity model of the crust of the Bohemian Massif, *Stud. Geophys. Geod.*, **56**, 249–267.
- Karousová, H., 2013. Teleseismic tomography of the upper mantle beneath the bohemian massif, *PhD thesis*, Department of Geophysics, Faculty of Mathematics and Physics, Charles University, Prague, Czech Republic.
- Karousová, H., Plomerová, J. & Babuška, V., 2013. Upper-mantle structure beneath the southern Bohemian Massif and its surroundings imaged by high-resolution tomography, *Geophys. J. Int.*, **194**, 1203–1215.
- Kennett, B. & Engdahl, R., 1991. Travel times for global earthquake location and phase identification, *Geophys. J. Int.*, **105**, 429–465.
- Kissling, E., 1988. Geotomography with local earthquake data, *Rev. Geophys.*, **26**, 659–698.
- Korja, A., Lahtinen, R. & Nironen, M., 2006. The Svekofennian orogen: a collage of microcontinents and island arcs, in *European Lithosphere Dynamics*, Vol. **32**, pp. 561–578, eds Gee, D.G. & Stephenson, R.A., Geol. Soc. London, Memoirs.
- Kozlovskaya, E., 2007. Seismic network XK: LAPNET/POLENET seismic temporary array (RESIF-SISMOP). RESIF - Réseau Sismologique et géodésique Français.
- Kustowski, B., Ekström, G. & Dziewoński, A.M., 2008. Anisotropic shear-wave velocity structure of the Earth's mantle: a global model, *J. geophys. Res.*, **113**, B06306.
- Lahtinen, R., Korja, A. & Nironen, M., 2005. Palaeoproterozoic tectonic evolution, in *The Precambrian Geology of Finland—Key to the Evolution of the Fennoscandian Shield*, pp. 418–532, eds Lehtinen, M., Nurmi, P.A. & Rämö, O.T., Elsevier.
- Lahtinen, R., Huhmaa, H., Lahayea, Y., Kousa, J. & Luukas, J., 2015. Archean-Proterozoic collision boundary in central Fennoscandia: revisited, *Precambrian Res.*, **261**, 127–165.
- Lippitsch, R., Kissling, E. & Ansorge, J., 2003. Upper mantle structure beneath the Alpine orogen from high-resolution teleseismic tomography, *J. geophys. Res.*, **108**, B82376.
- Liu, X. & Zhao, D., 2017. P-wave anisotropy, mantle wedge flow and olivine fabrics beneath Japan, *Geophys. J. Int.*, **210**, 1410–1431.
- Long, M.D. & Becker, T.W., 2010. Mantle dynamics and seismic anisotropy, *Earth planet. Sci. Lett.*, **297**, 341–354.
- Long, M.D. & Silver, P.G., 2009. Shear-wave splitting and mantle anisotropy: measurements, interpretations, and new directions, *Surv. Geophys.*, **30**, 407–461.
- Mainprice, D., 2007. Seismic anisotropy of the deep Earth from a mineral and rock physics perspective, in *Treatise on Geophysics*, pp. 437–491, ed Schubert, G., Elsevier.
- Maupin, V. & Park, J., 2007. Theory and observations—Wave propagation in anisotropic media, in *Treatise on Geophysics*, Vol. **1**: Seismology and the Structure of the Earth, pp. 289–321, eds Romanowicz, B. & Dziewonski, A., Elsevier.
- Menke, W., 1984. *Geophysical Data Analysis: Discrete Inverse Theory*, 1st edn, Academic Press, Inc.
- Munzarová, H., Plomerová, J., Babuška, V. & Vecsey, L., 2013. Upper-mantle fabrics beneath the Northern Apennines revealed by seismic anisotropy, *Geochem. Geophys. Geosyst.*, **14**, 1156–1181.
- Munzarová, H., Plomerová, J. & Kissling, E., 2018. Novel anisotropic teleseismic body-wave tomography code AniTomo to illuminate heterogeneous anisotropic upper mantle. Part I - Theory and inversion tuning with realistic synthetic data, *Geophys. J. Int.*, **215**, 524–545..
- Nita, B., Maurya, S. & Montagner, J.P., 2016. Anisotropic tomography of the European lithospheric structure from surface wave studies, *Geochem. Geophys. Geosyst.*, **17**, 2015–2033.
- Panning, M. & Romanowicz, B., 2006. A three-dimensional radially anisotropic model of shear velocity in the whole mantle, *Geophys. J. Int.*, **167**, 361–379.
- Park, J. & Levin, V., 2002. Seismic anisotropy: Tracing plate dynamics in the mantle, *Science*, **296**, 485–489.
- Pedersen, H., Debayle, E. & Maupin, V., the POLENET/LAPNET Working Group, 2013. Strong lateral variations of lithospheric mantle beneath cratons—example from the Baltic Shield, *Earth planet Sci. Lett.*, **383**, 164–172.
- Plomerová, J. & Babuška, V., 2010. Long memory of mantle lithosphere fabric—European LAB constrained from seismic anisotropy, *Lithos*, **120**, 131–143.
- Plomerová, J., Babuška, V., Kozlovskaya, E., Vecsey, L. & Hyvonen, L.T., 2008. Seismic anisotropy—a key to resolve fabrics of mantle lithosphere of Fennoscandia, *Tectonophysics*, **462**, 125–136.
- Plomerová, J., Babuška, V., Vecsey, L., Kozlovskaya, E. & Raita, T., SSTWG, 2006. Proterozoic-Archean boundary in the upper mantle of eastern Fennoscandia as seen by seismic anisotropy, *J. Geodyn.*, **41**, 400–410.
- Plomerová, J., Munzarová, H., Vecsey, L., Kissling, E., Achauer, U. & Babuška, V., 2016. Cenozoic volcanism in the Bohemian Massif in the context of P-and S-velocity high-resolution teleseismic tomography of the upper mantle, *Geochem. Geophys. Geosyst.*, **17**(8), 3326–3349.
- Plomerová, J., Vecsey, L. & Babuška, V., 2012. Mapping seismic anisotropy of the lithospheric mantle beneath the northern and eastern Bohemian Massif (central Europe), *Tectonophysics*, **564–565**, 38–53.
- Plomerová, J., Vecsey, L. & Babuška, V., LAPNET working group, 2011. Domains of Archean mantle lithosphere deciphered by seismic anisotropy— inferences from the LAPNET array in northern Fennoscandia, *Solid Earth*, **2**, 303–313.
- Sandoval, S., Kissling, E. & Ansorge, J., SVEKALAPKO Seismic Tomography working Group, 2004. High-resolution body wave tomography beneath the SVEKALAPKO array—II. Anomalous upper mantle structure beneath the central Baltic Shield, *Geophys. J. Int.*, **157**, 200–214.
- Savage, M.K., 1999. Seismic anisotropy and mantle deformation: what have we learned from shear wave splitting?, *Rev. Geophys.*, **37**, 65–106.
- Shomali, Z.H., Roberts, R.G. & Pedersen, L.B., the TOR Working Group, 2006. Lithospheric structure of the Tornquist Zone resolved by nonlinear P and S teleseismic tomography along the TOR array, *Tectonophysics*, **416**, 133–149.
- Šílený, J. & Plomerová, J., 1996. Inversion of shear-wave splitting parameters to retrieve three-dimensional orientation of anisotropy in continental lithosphere, *Phys. Earth planet. Inter.*, **95**, 277–292.
- Silvennoinen, H., Kozlovskaya, E. & Kissling, E., 2016. POLENET/LAPNET teleseismic P wave travel time tomography model of the upper mantle beneath northern Fennoscandia, *Solid Earth*, **7**, 425–439.
- Silvennoinen, H., Kozlovskaya, E., Kissling, E. & Kosarev, G., POLENET/LAPNET working group, 2014. A new Moho boundary map

- for northern Fennoscandian shield based on combined controlled-source seismic and receiver function data, *Geophys. Res. J.*, **1/2**, 19–32.
- Silver, P.G., 1996. Seismic anisotropy beneath the continents: probing the depths of geology, *Annu. Rev. Earth planet. Sci.*, **24**, 385–432.
- Slagstad, T., Balling, N., Elvebakken, H., Midttømme, K., Olesen, O., Olsen, L. & Pascal, C., 2009. Heat-flow measurements in Late Palaeoproterozoic to Permian geological provinces in south and central Norway and a new heat-flow map of Fennoscandia and the Norwegian “Greenland Sea”, *Tectonophysics*, **473**, 341–361.
- SNSN, 1904. Swedish National Seismic Network. Uppsala University, Uppsala, Sweden. Other/Seismic network.
- Snyder, D.B., 2002. Lithospheric growth at margins of cratons, *Tectonophysics*, **355**, 7–22.
- Stammler, K., 1993. Seismic handler programmable multichannel data handler for interactive and automatic processing of seismological analyses, *Comput. Geosci.*, **19**, 135–140.
- Steck, L.K. & Prothero, W.A., 1991. A 3-D raytracer for teleseismic body-wave arrival times, *Bull. seism. Soc. Am.*, **81**, 1332–1339.
- Vecsey, L., Plomerová, J., Kozlovskaya, E. & Babuška, V., 2007. Shear-wave splitting as a diagnostic of varying upper mantle structure beneath south-eastern Fennoscandia, *Tectonophysics*, **438**, 57–77.
- Vinnik, L., Kozlovskaya, E., Oreshin, S., Kosarev, G., Piiponen, K. & Silvenoinen, H., 2016. The lithosphere, LAB, LVZ and Lehmann discontinuity under central Fennoscandia from receiver functions, *Tectonophysics*, **667**, 189–198.
- Vinnik, L., Oreshin, S., Makeyeva, L. & Kozlovskaya, E., POLENET/LAPNET Working Group, 2014. Anisotropic lithosphere below Fennoscandia from receiver functions and SKS waveforms of POLENET/LAPNET array, *Tectonophysics*, **628**, 45–54.
- Wang, J. & Zhao, D., 2013. P-wave tomography for 3-D radial and azimuthal anisotropy of Tohoku and Kyushu subduction zones, *Geophys. J. Int.*, **193**, 1166–1181.
- Wessel, P. & Smith, W.H.F., 1998. New, improved version of the generic mapping tools released, *EOS, Trans. Am. Geophys. Un.*, **79**, 579.
- Weihed, P., Arndt, N., Billström, K., Duchesne, J.C., Eilu, P., Martinsson, O., Papunen, H. & Lahtinen, R., 2005. 8: Precambrian geodynamics and ore formation: the Fennoscandian Shield, *Ore Geol. Rev.*, **27**, 273–322.
- Weiland, C.M., Steck, L.K., Dawson, P.B. & Korneev, V.A., 1995. Nonlinear teleseismic tomography at Long Valley caldera, using three-dimensional minimum travel time ray tracing, *J. geophys. Res.*, **100**, 20379–20390.
- Yuan, K. & Beghein, C., 2014. Three-dimensional variations in Love and Rayleigh wave azimuthal anisotropy for the upper 800 km of the mantle, *J. geophys. Res.: Solid Earth*, **119**, 3232–3255.
- Zhu, H., Bozdağ, E. & Tromp, J., 2014. Seismic structure of the European upper mantle based on adjoint tomography, *Geophys. J. Int.*, **201**, 18–52.

SUPPORTING INFORMATION

Supplementary data are available at [GJI](#) online.

Figure S1. Diagonal elements of resolution matrix evaluated according to eq. (4) for the ray geometry of the LAPNET data set and the final parametrization of the volume studied with a denser vertical spacing at the top part. Dotted white curve marks smoothed contour of RDE equal to 0.5. The relatively small area delimited by the 0.5 contour at the 50 km depth is caused by denser vertical grid spacing in this part of the model. Red line delimits a region where inversion for all four anisotropic parameters is allowed, while inversion just for the purely isotropic-velocity perturbations is allowed within volume contoured by black line (see Figs 3 and S3). Triangles represent seismic stations of experiment LAPNET.

Figure S2. Ray paths at the individual depth layers of model parametrization. Dashed black curve marks smoothed contour of RDE equal to 0.5. Red line delimits a region where inversion for all the four anisotropic parameters is allowed, while inversion just for the purely isotropic-velocity perturbations is allowed in a larger

region, marked by blue line (see Figs 3 and S3). Triangles represent seismic stations of experiment LAPNET.

Figure S3. Ray density tensors (RDT) evaluated at the parametrization nodes of all the depths for the ray distribution of the LAPNET data set. See caption of Fig. 3 for details.

Figure S4. Anisotropic-velocity model retrieved by the coupled anisotropic-isotropic tomography. On the left, there are all individual solutions of the anisotropic part of the model displayed at each parametrization node (see Fig. 5 for details). Only individual solutions with strength of anisotropy larger than 1 per cent at nodes with at least eight individual solutions larger than 1 per cent are plotted. On the background, the isotropic-velocity perturbations as in Fig. 6 are displayed. On the right, we present the anisotropic velocities averaged from the set of individual solutions. See Figs 5 and 7 for details.

Figure S5. P-wave isotropic-velocity perturbations retrieved by the isotropic version of the AniTomo code. Part of the model with $RDE < 0.5$ is shaded. Red dashed line marks the region with relatively low-velocity perturbations that dominates the model at depths of 80, 120 and 170 km. The hatched area locates a zone of weaker anisotropy and velocity perturbations within Region III at depth of 120 km. Distribution of the isotropic-velocity perturbations from the purely isotropic inversion and from the set of the coupled anisotropic-isotropic inversions (Fig. 6) are the same, in general. The brown dashed curves mark boundaries of cratonic provinces after Korja *et al.* (2006); see also Fig. 1.

Figure S6. Standard deviations of the isotropic-velocity perturbations evaluated at each grid node from the set of 24 coupled anisotropic-isotropic inversions with different initial orientations of the symmetry axis. The standard deviations are lower than 1 per cent at almost all the grid nodes and they are even lower than 0.5 per cent in majority of the nodes. Triangles represent seismic stations of experiment LAPNET together with the nearby permanent stations.

Figure S7. Anisotropic-velocity model retrieved by the coupled anisotropic-isotropic tomography code for the synthetic test mimicking a realistic anisotropic structure of the mantle lithosphere. See caption of Fig. 8 for details.

Figure S8. Anisotropic-velocity model at 120 km depth from a set of synthetic tests that follows the three-block structure (see Fig. S7), but with different characteristics of the blocks (schematic insets in the lower left corners). Perturbations of the isotropic velocities in the blocks with non-zero deviation from the IASP'91 model are set to 3 per cent amplitude. Strength of anisotropy in the anisotropic blocks is always 5 per cent. See captions of Figs 7 and 5 for description of plotting the output anisotropic parameters. Dotted black curve marks smoothed contour of RDE equal to 0.5.

Figure S9. P spheres showing directional distribution of relatively early and delayed P-wave arrival times at the individual stations of the extended LAPNET array. The stations are clustered into the domains according to similarity of their P-sphere patterns (see Fig. 9 for details). The P spheres exhibiting only a tendency to the typical pattern of the corresponding domain are marked by a dashed frame.

Figure S10. Anisotropic-velocity model from a synthetic test designed to investigate capability of the LAPNET ray geometry to resolve a vertically variable anisotropy. The synthetic model includes two 5 per cent anisotropic blocks with different orientation of symmetry axes. The upper one is at depths of 80 and 120 km with axis azimuth of 300° and inclination of 40° . The lower block is at depths of 170 and 220 km with axis azimuth of 60° and inclination of 60° . See caption of Figs 5 and 7 for description of plotting the

output anisotropic parameters. Dotted black curve marks smoothed contour of RDE equal to 0.5.

Figure S11. Vertical cross-section through the model of the isotropic-velocity perturbations from the coupled anisotropic-isotropic tomography along the 66°N latitude. Parts of the model with $RDE < 0.5$ and the depths corresponding to the crust are shaded. Red dashed line marks the westward dipping boundary of

the relatively low-velocity perturbations dominating the western part of the model at depths of 80, 120 and 170 km (see also Figs 6 and 7).

Please note: Oxford University Press is not responsible for the content or functionality of any supporting materials supplied by the authors. Any queries (other than missing material) should be directed to the corresponding author for the article.